

# Spatiotemporal Imaging with Diffeomorphic Optimal Transportation

Chong Chen\*

## Abstract

We propose a variational model with diffeomorphic optimal transportation for joint image reconstruction and motion estimation. The proposed model is a production of assembling the Wasserstein distance with the Benamou–Brenier formula in optimal transportation and the flow of diffeomorphisms involved in large deformation diffeomorphic metric mapping, which is suitable for the scenario of spatiotemporal imaging with large diffeomorphic and mass-preserving deformations. Specifically, we first use the Benamou–Brenier formula to characterize the optimal transport cost among the flow of mass-preserving images, and restrict the velocity field into the admissible Hilbert space to guarantee the generated deformation flow being diffeomorphic. We then gain the ODE-constrained equivalent formulation for Benamou–Brenier formula. We finally obtain the proposed model with ODE constraint following the framework that presented in our previous work. We further get the equivalent PDE-constrained optimal control formulation. The proposed model is compared against several existing alternatives theoretically. The alternating minimization algorithm is presented for solving the time-discretized version of the proposed model with ODE constraint. Several important issues on the proposed model and associated algorithms are also discussed. Particularly, we present several potential models based on the proposed diffeomorphic optimal transportation. Under appropriate conditions, the proposed algorithm also provides a new scheme to solve the models using quadratic Wasserstein distance. The performance is finally evaluated by several numerical experiments in space-time tomography, where the data is measured from the concerned sequential images with sparse views and/or various noise levels.

**Keywords:** spatiotemporal imaging, joint image reconstruction and motion estimation, quadratic Wasserstein distance, flow of diffeomorphisms, diffeomorphic optimal transportation, mass-preserving deformation

## 1 Introduction

Mathematically, the spatiotemporal (space-time) imaging is typically a kind of time-dependent or dynamic inverse problems, which has been gained extensively study ([25, 50, 16] and the references therein). As a representative example, when the tomographic imaging (e.g., computed tomography (CT), positron emission tomography (PET), single photon emission computed tomography (SPECT), Magnetic Resonance Imaging (MRI)) is used for chest or heart inspection, the measurements are frequently acquired over a time period in the minute magnitude. If the unavoidable respiration and/or cardiac movements are neglected or failed to track and correct, this would lead to the reconstructed images with severe degradation [56, 51, 31, 47]. As a result,

---

\*LSEC, ICMSEC, Academy of Mathematics and Systems Science, Chinese Academy of Sciences, Beijing 100190, China (chench@lsec.cc.ac.cn).

it is significant to estimate and compensate for the unknown motions of the organs during image reconstruction in spatiotemporal imaging.

In spatiotemporal imaging, the acquired data is usually a time-series, which is often divided into gates by time or amplitude based respiration and/or cardiac gating method. The details about the gating method are referred to [36, 19, 21, 39, 29]. After gated, the collected data within each gate can be seen as a certain data measured from a static object in a fixed time or pseudo-time state [15]. Then one can use the different kind of strategies to perform spatiotemporal image reconstruction. An intuitive strategy is first performing image reconstruction for each gate independently, and then implementing motion correction/compensation by image registration for the reconstructed images [18, 20, 4, 26, 9]. However, the data at each gate is often interfered by enhanced noise levels due to gating. If it is worse sparse-sampled in order to decrease the radiative dose, then the reconstructed images at the first step would be reduced quality or full of artifacts, which makes the following motion correction step almost malfunction. The other strategy is joint image reconstruction and motion estimation, namely, incorporating the physical motion into the reconstruction process, in which one establishes multiple tasks jointly into one single model, and then gains the optimal solution to reconstruct the image at each gate. The main idea of this type of methods is to make use of the sufficient information in the data for each step. A lot of approaches have been proposed for how to do this, such as those in [49, 10, 7, 32, 52, 38, 8, 12, 13, 40, 16]. Additionally, several methods took the spatiotemporal images as the unknowns of the optimization/variational models, and considered the temporal regularization by locally adjacent images or in sparse matrix form [31, 33, 24, 48].

In particular, a general framework of joint variational model was proposed for spatiotemporal imaging in [16]. Actually, the most important component of that model is for motion estimation using the acquired projection data under the assumption that the template is given. This problem is termed sequentially indirect image registration, which is the generalization of indirect image registration studied in [17]. More details on the latter are referred to [45, 28]. To solve the former, a consistent growth model based on large deformation diffeomorphic metric mapping (LDDMM) was proposed in [16], which can track the flow of motions with large non-rigid and diffeomorphic deformations. It is well-known that the LDDMM is a fundamental method for diffeomorphic image registration ([54, 22, 42, 5, 58, 11]).

Following the general framework presented in [16], the current work is dedicated to proposing a new joint variational model with diffeomorphic optimal transportation, which is useful for the spatiotemporal imaging with large mass-preserving and diffeomorphic deformations. The mass-preserving property was often considered to be significant in dynamic PET imaging, such as the cardiac imaging [26]. To do so, being quite different from the method in [16], this paper uses the the Wasserstein distance with Benamou–Brenier formula in optimal transportation to characterize the optimal transport cost among the mass-preserving image flows. For the detailed introduction on the theory and applications of optimal transportation, the readers are referred to [6, 55, 1, 30, 23, 41, 2, 35, 46]. Furthermore, this work restricts the unknown velocity field into the admissible Hilbert space to generate the flow of diffeomorphisms for tracking the involved motions. Numerically, the alternating minimization algorithm is presented for solving the proposed model with ordinary differential equation (ODE) constraint. Moreover, under appropriate conditions, the proposed algorithm provides a new method to solve the models using  $\mathcal{L}^2$  Wasserstein distance in Benamou–Brenier formulation, such as the extended models with diffeomorphic optimal transportation for (sequential) image registration and the related indirect problems.

The outline of this paper is organized as follows. Section 2 introduces the required mathematical preliminaries. The new variational model for joint image reconstruction and motion estimation is presented in section 3. The numerical implementation is given in section 4 to solve

the proposed model. The numerical test suites are performed in section 5 to evaluate the performance of the proposed method. Section 6 further discusses several important issues about the proposed model and related algorithms. Finally, the paper is concluded by section 7.

## 2 Preliminaries

First of all, we present the problem setting of spatiotemporal imaging. And then we recall the requisite mathematical tools, including the basic concept and related results of Wasserstein distance in optimal transportation, and the flow of diffeomorphisms in LDDMM.

### 2.1 Spatiotemporal imaging

A general framework for spatiotemporal imaging was presented in the previous work [16], which is based on the deformable template of shape theory [53, 27, 58]. Here we will give a brief introduction.

Suppose that the time-dependent image required to be reconstructed is defined by

$$f: [t_0, t_1] \times \Omega \rightarrow \mathbb{R}^m,$$

where  $m$  (generally  $m = 1$ ) is denoted as the modality number,  $[t_0, t_1] \subset \mathbb{R}^1$  is expressed as the temporal domain, and  $\Omega \subset \mathbb{R}^n$  (often  $n = 2$  or  $3$ ) is represented as the spatial domain. The domain  $\Omega$  is assumed to include the support of the images for all of the time, which is a bounded, compact, convex open set with the strong local Lipschitz condition throughout the paper. Note that the general (pseudo) time domain  $[t_0, t_1]$  can be always reparameterized onto  $[0, 1]$ . It is well-known that the aim of spatiotemporal imaging is to reconstruct a time-dependent image  $f(t, \cdot) \in \mathcal{X}$  by using the acquired data  $g(t, \cdot) \in \mathcal{Y}$  for  $t \in [0, 1]$ , where  $\mathcal{X}$  denotes the reconstruction function space, and  $\mathcal{Y}$  represents the data function space. Correspondingly, the general mathematical formulation is written as

$$g(t, \cdot) = \mathcal{T}(t, f(t, \cdot)) + g_{\text{noise}}(t, \cdot) \quad \text{for } t \in [0, 1]. \quad (1)$$

Here the  $\mathcal{T}(t, \cdot): \mathcal{X} \rightarrow \mathcal{Y}$  represents a time-dependent linear or nonlinear forward operator, which models the forward process without noise or errors on how the image at time state  $t$  generates the data. For instance, the forward operator is realized by Radon transform in CT and attenuation-corrected (AC) PET; the attenuated Radon transform is adopted by SPECT; the downsampled Fourier transform is used for MRI [37, 44]. For brevity, we denote  $\mathcal{T}(t, \cdot)$  by  $\mathcal{T}_t$ . Moreover, the  $g_{\text{noise}}(t, \cdot) \in \mathcal{Y}$  stands for the uncertain noise contained in data,

As in [16], based on the deformable template of shape theory, the time-dependent image can be expressed as

$$f(t, \cdot) := \mathcal{W}(\phi_t, I), \quad (2)$$

where  $\mathcal{X} \ni I: \Omega \rightarrow \mathbb{R}$  denotes the template that is time-independent spatial component of the spatiotemporal image,  $\mathcal{G} \ni \phi_t: \Omega \rightarrow \Omega$  defines the time-dependent deformation that manages the temporal evolution of the template, and the  $\mathcal{G}$  stands for the group of diffeomorphisms on  $\Omega$ . The  $\mathcal{W}: \mathcal{G} \times \mathcal{X} \rightarrow \mathcal{X}$  denotes the temporal evolution operator, which is required to be a group action of  $\mathcal{G}$  on  $\mathcal{X}$ . For short, we rewrite  $\mathcal{W}(\phi_t, I) := \phi_t.I$ . In other words, given the template  $I$  and the deformation  $\phi_t$ , the spatiotemporal image at time  $t$  can be generated by  $f(t, \cdot) = \phi_t.I$ . Remark that  $\phi_0 = \text{Id}$  often denotes the identity deformation (mapping). By (2), the spatiotemporal imaging (1) can be translated into

$$g(t, \cdot) = \mathcal{T}_t(\phi_t.I) + g_{\text{noise}}(t, \cdot) \quad \text{for } t \in [0, 1]. \quad (3)$$

There exist two frequently used group actions [17]. The one that adopted in this work is given by the form of mass-preserving deformation

$$\phi_t.I = |D(\phi_t^{-1})|I \circ \phi_t^{-1}, \quad (4)$$

where the “ $\circ$ ” denotes function composition, and  $|D(\phi)|$  is referred to the determinant of the Jacobian of  $\phi$ . Obviously, this deformation changes the intensity of the image but preserves its mass. It is well-known that such deformation is required in the framework of optimal transportation. An alternative one is given by geometric deformation, which is referred to [17].

As proposed in [16], the general framework for solving the spatiotemporal inverse problem is formulated as

$$\min_{\substack{I \in \mathcal{X} \\ \phi_t \in \mathcal{G}}} \int_0^1 \left[ \mathcal{D}_{\mathcal{T}_t, g_t}(\phi_t.I) + \mu_2 \mathcal{R}_2(\phi_t) \right] dt + \mu_1 \mathcal{R}_1(I), \quad (5)$$

where

$$\mathcal{D}_{\mathcal{T}_t, g_t}(\phi_t.I) := \mathcal{D}\left(\mathcal{T}_t(\phi_t.I), g(t, \cdot)\right) \quad (6)$$

and  $\mu_1, \mu_2$  are positive regularization parameters. Here the  $\mathcal{D}: \mathcal{Y} \times \mathcal{Y} \rightarrow \mathbb{R}_+$  acts as the data fitting functional. The  $\mathcal{R}_1: \mathcal{X} \rightarrow \mathbb{R}_+$  is the spatial regularization for imposing priori information about the template image. Moreover, the  $\mathcal{R}_2: \mathcal{G} \rightarrow \mathbb{R}_+$  is the shape regularization for constructing the desirable and applicable flow of deformations, which is critical in mathematical modelling for spatiotemporal imaging.

In this work, we will study this problem by combining the Wasserstein distance and the flow of diffeomorphisms.

## 2.2 The Wasserstein distance

The original transportation problem can be traced back to the work of Monge in [43], which is a civil engineering problem that parcels of materials have to be displaced from one site to another one with minimal transportation cost [6]. A modern treatment of this problem has been initiated by Kantorovich in [34], leading to the Monge–Kantorovich problem which has gained extensive interests, and also had a broad range of applications in the recent years [6, 55, 1].

The original problem can be stated as follows: given two density distributions  $f_0$  and  $f_1$  with equal masses of a given material (corresponding for instance to an embankment and an excavation), find a transportation map  $\phi: \mathbb{R}^n \rightarrow \mathbb{R}^n$  which carries the first distribution into the second and minimizes the transportation cost

$$d_p(f_0, f_1) := \inf_{\phi} \left( \int_{\mathbb{R}^n} |x - \phi(x)|^p f_0(x) dx \right)^{1/p}, \quad (7)$$

where the condition that the first distribution of mass is carried into the second can be written as

$$\int_{\phi^{-1}(B)} f_0(x) dx = \int_B f_1(y) dy \quad \text{for } \forall B \subset \mathcal{B}(\mathbb{R}^n), \quad (8)$$

or, by the change of variables formula, as

$$|D(\phi)(x)| f_1(\phi(x)) = f_0(x) \quad \text{for } \mathcal{L}^n\text{-a.e. } x \in B, \quad (9)$$

namely, the *Jacobian equation* (similarly, see the mass-preserving deformation in (4)), if  $\phi$  is one to one and sufficiently regular. Here  $d_p(f_0, f_1)$  is defined as the so-called  $\mathcal{L}^p$  *Wasserstein (or Kantorovich) distance* between  $f_0$  and  $f_1$  with fixed  $p \geq 1$ , in which  $|\cdot|$  denotes the Euclidean

norm in  $\mathbb{R}^n$ , and the infimum is taken among all map  $\phi$  transporting  $f_0$  to  $f_1$ . Note that  $\mathcal{B}(\mathbb{R}^n)$  is Borel  $\sigma$ -algebra of  $\mathbb{R}^n$ , and  $\mathcal{L}^n$  is Lebesgue measure in  $\mathbb{R}^d$ . If the infimum is achieved by some map  $\phi^*$ , we say that  $\phi^*$  is an optimal transfer and solves the  $\mathcal{L}^p$  Monge–Kantorovich problem (MKP) [6, 1].

For the case  $p = 2$ , the above optimal transportation problem can be further reformulated in the way inspired by fluid mechanics, which will be useful for the study of spatiotemporal imaging.

**Theorem 1** ([6]). *Assume that the time-dependent density  $f(t, x) \geq 0$  and velocity field  $\boldsymbol{\nu}(t, x) \in \mathbb{R}^n$  are appropriately smooth, and  $f_0$  and  $f_1$  are compactly supported. The square of the  $\mathcal{L}^2$  Wasserstein distance equals to*

$$\inf_{f \geq 0, \boldsymbol{\nu}} \int_0^1 \int_{\mathbb{R}^n} f(t, x) |\boldsymbol{\nu}(t, x)|^2 dx dt, \quad (10)$$

such that

$$\begin{cases} \partial_t f(t, x) + \nabla \cdot (f(t, x) \boldsymbol{\nu}(t, x)) = 0 \\ f(0, x) = f_0(x), \quad f(1, x) = f_1(x) \end{cases} \quad \text{for } x \in \mathbb{R}^n \text{ and } 0 \leq t \leq 1. \quad (11)$$

The formula in theorem 1 is also called *Benamou–Brenier formula*, which is referred to [55, Theorem 8.1]. Remarkably, the minimizer of  $\mathcal{L}^2$  MKP is the solution at  $t = 1$  to the following ODE

$$\begin{cases} \partial_t \phi_t(x) = \boldsymbol{\nu}(t, \phi_t(x)) \\ \phi_0(x) = x \end{cases} \quad \text{for } x \in \mathbb{R}^n \text{ and } 0 \leq t \leq 1. \quad (12)$$

### 2.3 The flow of diffeomorphisms

To begin with, let  $f_0$  and  $f_1$  be two density functions compactly supported on  $\Omega$ . Here we review a way to produce a flow of diffeomorphisms through a velocity field, which has been successfully used in LDDMM [5, 58]. Specifically, fixed an appropriate velocity field  $\boldsymbol{\nu}: [0, 1] \times \Omega \rightarrow \mathbb{R}^n$ , a flow of diffeomorphisms  $\phi_t$  is produced by the ODE below.

$$\begin{cases} \partial_t \phi_t(x) = \boldsymbol{\nu}(t, \phi_t(x)) \\ \phi_0(x) = x \end{cases} \quad \text{for } x \in \Omega \text{ and } 0 \leq t \leq 1. \quad (13)$$

Subsequently, the required regularity condition will be given for the velocity field. To proceed, we first give the concept of admissible space.

**Definition 1** ([58]). If a Hilbert space  $\mathcal{V}$  is (canonically) embedded in  $\mathcal{C}_0^1(\Omega, \mathbb{R}^n)$  with norm  $\|\cdot\|_{1, \infty}$ , namely, existing a constant  $C > 0$  such that

$$\|\nu\|_{1, \infty} \leq C \|\nu\|_{\mathcal{V}} \quad \text{for any } \nu \in \mathcal{V},$$

then the  $\mathcal{V}$  is called admissible. Here  $\|\nu\|_{1, \infty} := \|\nu\|_{\infty} + \|D\nu\|_{\infty}$  for  $\nu \in \mathcal{C}_0^1(\Omega, \mathbb{R}^n)$ .

Using the definition of definition 1, a space of velocity fields is defined as

$$\mathcal{L}^p([0, 1], \mathcal{V}) := \left\{ \boldsymbol{\nu} : \boldsymbol{\nu}(t, \cdot) \in \mathcal{V} \text{ and } \|\boldsymbol{\nu}\|_{\mathcal{L}^p([0, 1], \mathcal{V})} < \infty \text{ for } 1 \leq p \leq \infty. \right\} \quad (14)$$

Then the norm is given as

$$\|\boldsymbol{\nu}\|_{\mathcal{L}^p([0, 1], \mathcal{V})} := \left( \int_0^1 \|\boldsymbol{\nu}(t, \cdot)\|_{\mathcal{V}}^p dt \right)^{1/p}.$$

For simplicity, denote  $\mathcal{L}^p([0, 1], \mathcal{V})$  by  $\mathcal{L}_{\mathcal{V}}^p$ . Particularly, for  $p = 2$ , the  $\mathcal{L}_{\mathcal{V}}^2$  is a Hilbert space, the inner product of which is defined as

$$\langle \nu, \eta \rangle_{\mathcal{L}_{\mathcal{V}}^2} = \int_0^1 \langle \nu(t, \cdot), \eta(t, \cdot) \rangle_{\mathcal{V}} dt \quad \text{for } \nu, \eta \in \mathcal{L}_{\mathcal{V}}^2.$$

More importantly, if the given velocity field is included in  $\mathcal{L}_{\mathcal{V}}^2$ , a flow of diffeomorphisms can be obtained immediately. This result is given by the following theorem.

**Theorem 2** ([58, 11]). *Let  $\mathcal{V}$  be an admissible Hilbert space, and the given  $\nu \in \mathcal{L}_{\mathcal{V}}^2$  be a velocity field. Then the ODE (13) has a unique solution  $\phi^{\nu} \in \mathcal{C}^1([0, 1] \times \Omega, \Omega)$ , and for  $t \in [0, 1]$ , the mapping  $\phi_t^{\nu} : \Omega \rightarrow \Omega$  is a  $\mathcal{C}^1$ -diffeomorphism on  $\Omega$ .*

### 3 Spatiotemporal imaging with diffeomorphic optimal transportation

This section proposes a joint variational model based on the thought here termed diffeomorphic optimal transportation.

Although the minimizer for  $\mathcal{L}^2$  MKP is expected to be one to one and sufficiently regular, the formula of interest cannot restrict it into the space with such regularity. As we know in section 2.3, the definition 1 and theorem 2 give us the inspiration on the regularity (i.e., admissible Hilbert space) that is required for the velocity field to generate a flow of diffeomorphisms by the ODE (13). One method to ensure a Hilbert space being admissible is to construct the space via a differential operator  $L$  (denoting its adjoint as  $L^{\dagger}$ ) given by

$$\langle \nu, \eta \rangle_{\mathcal{V}} := \langle L\nu, L\eta \rangle_{\mathcal{L}^2} = \langle L^{\dagger}L\nu, \eta \rangle_{\mathcal{L}^2}, \quad (15)$$

where  $\mathcal{L}^2$  denotes the usual inner product space with square integrable vector fields defined on  $\Omega$ .

The way of choice for  $L$  is referred to [11, Example 18]. For  $m > n/2 + 1$ , the space  $H^m(\Omega)$  is an admissible space. However, the  $L$  is usually complex that difficultly be used in practice.

*Remark 1.* A kind of admissible Hilbert spaces is reproducing kernel Hilbert space (RKHS), which is affiliated with a symmetric and positive-definite reproducing kernel [3, 58]. Assume that the  $\mathcal{V}$  is an RKHS with a reproducing kernel  $\mathsf{K} : \Omega \times \Omega \rightarrow \mathbb{M}_+^{d \times d}$ . And then a compactly self-adjoint operator  $\mathcal{K} : \mathcal{L}^2(\Omega, \mathbb{R}^n) \rightarrow \mathcal{V}$  is uniquely defined by

$$\langle \nu, \eta \rangle_{\mathcal{L}^2} = \langle \mathcal{K}(\nu), \eta \rangle_{\mathcal{V}},$$

where  $\mathcal{K}(\nu) = \int_{\Omega} \mathsf{K}(\cdot, y)\nu(y)dy$ . Combined with (15), the fact for  $\nu \in \mathcal{V}$  is that

$$\mathcal{K}(L^{\dagger}L)\nu = \nu. \quad (16)$$

Consequently, if the RKHS is taken into account, the reproducing kernel would be used rather than the  $L$  needs to be given explicitly. In what follows the space of vector fields is selected as the RKHS with Gaussian reproducing kernel for the advantages of sufficient smoothness and fast computability [16].

#### 3.1 The proposed model

Here we propose the variational model for joint image reconstruction and motion estimation in spatiotemporal imaging.

To guarantee the flow of deformations being diffeomorphic, we restrict the velocity field  $\nu$  into the admissible Hilbert space  $\mathcal{L}_{\mathcal{V}}^2$ , namely,  $\nu \in \mathcal{L}_{\mathcal{V}}^2$ . By theorem 2, the unique solution, denoted by  $\phi_t^\nu$  for  $0 \leq t \leq 1$ , to the ODE (13) is determined by the given velocity field  $\nu$ , which is a flow of  $\mathcal{C}^1$ -diffeomorphisms with  $\phi_0^\nu = \text{Id}$ . For ease of description, we adopt the convention

$$\phi_{s,t}^\nu := \phi_t^\nu \circ (\phi_s^\nu)^{-1} \quad \text{for } 0 \leq t, s \leq 1. \quad (17)$$

Using (17), we have

$$\phi_t^\nu = \phi_{0,t}^\nu, \quad (\phi_t^\nu)^{-1} = \phi_{t,0}^\nu. \quad (18)$$

Subsequently, we state a significant result by the following theorem.

**Theorem 3.** *Assume that the time-dependent density function  $f(t, x) \geq 0$  is appropriately smooth, the  $\mathcal{V}$  is an admissible Hilbert space, the velocity field  $\nu \in \mathcal{L}_{\mathcal{V}}^2$ , and  $f_0, f_1$  are compactly supported on  $\Omega$ . The Benamou–Brenier formula in theorem 1 is equivalent to*

$$\inf_{\substack{\nu \in \mathcal{L}_{\mathcal{V}}^2 \\ \phi_{0,1}^\nu, I=f_1, I \geq 0}} \int_0^1 \int_{\Omega} \phi_{0,t}^\nu \cdot I(x) |\nu(t, x)|^2 dx dt \quad (19)$$

s.t.  $\phi_{0,t}^\nu$  solves ODE (13),

where  $I = f_0$ .

*Proof.* Suppose that  $f$  and  $\nu$  solve (10). Define the diffeomorphism  $\psi(t, \cdot)$  that solves the ODE (13) with the given  $\nu$ . Since  $f$  satisfies the partial differential equation (PDE) constraint in (11), considering  $t \mapsto |D\psi(t, \cdot)|f(t, \psi(t, \cdot))$ , we have

$$\begin{aligned} \frac{d}{dt} \left( |D\psi(t, \cdot)|f(t, \psi(t, \cdot)) \right) \\ = |D\psi(t, \cdot)| \left[ \frac{d}{dt} f(t, \cdot) + \text{div} \left( f(t, \cdot) \nu(t, \cdot) \right) \right] (\psi(t, \cdot)) = 0. \end{aligned} \quad (20)$$

Hence,  $t \mapsto |D\psi(t, \cdot)|f(t, \psi(t, \cdot))$  is constant so in particular we have

$$|D\psi(t, \cdot)|f(t, \psi(t, \cdot)) \equiv f(0, \cdot) = I.$$

Let  $\psi_t$  be  $\phi_{0,t}^\nu$ . Then  $f(t, \cdot) = \phi_{0,t}^\nu \cdot I$ . Hence a solution to (10) produces a solution to (19). It is simple to verify that a solution to (19) also produces a solution to (10).  $\square$

Actually, the (13) is the characteristic ODE of the PDE (11). Note that the (19) implies that the distance between  $f_0$  and  $f_1$  can be seen as the transportation cost from  $f_0$  to  $f_1$  that characterized by the velocity field  $\nu(t, \cdot)$  for  $0 \leq t \leq 1$ . And the velocity field  $\nu(t, \cdot)$  with  $t$  from 0 to 1 generates the flow of diffeomorphisms  $\phi_{0,t}^\nu$ , combined with  $I \geq 0$ , which leads to  $f(t, \cdot) = \phi_{0,t}^\nu \cdot I$  also with compact support  $\Omega$  and nonnegativity.

Inspired by the formulation in (19) and the strategy in [16], we construct the shape regularization  $\mathcal{R}_2$  for the temporal deformation  $\phi_t^\nu$  by

$$\mathcal{R}_2(\phi_t^\nu) := \int_0^t \int_{\Omega} \phi_{0,\tau}^\nu \cdot I(x) |\nu(\tau, x)|^2 dx d\tau, \quad (21)$$

where the available  $\phi_{0,\tau}^\nu \cdot I$  is incorporated into the formula above as a weight function. Hence the proposed model with ODE constraint under the framework in (5) is formulated as

$$\begin{aligned} \min_{\substack{I \in \mathcal{X} \\ \nu \in \mathcal{L}_{\mathcal{V}}^2}} \int_0^1 \left[ \mathcal{D}_{\mathcal{T}_t, g_t}(\phi_{0,t}^\nu \cdot I) + \mu_2 \int_0^t \int_{\Omega} \phi_{0,\tau}^\nu \cdot I(x) |\nu(\tau, x)|^2 dx d\tau \right] dt + \mu_1 \mathcal{R}_1(I) \\ \text{s.t. } \phi_{0,t}^\nu \text{ solves ODE (13),} \end{aligned} \quad (22)$$

where  $\mathcal{X}$  denotes a certain space of real-valued functions with appropriate smoothness and nonnegativity.

The model (22) is termed *time-continuous version* of the proposed model with ODE constraint. Furthermore, this model can be restated as a PDE-constrained optimal control formulation, which is given by the following theorem.

**Theorem 4.** *Assume that  $\mathcal{X}$  is a space of nonnegative real-valued functions with appropriate smoothness and compactly supported on  $\Omega$ . Let  $I \in \mathcal{X}$  and  $f(t, \cdot) := \phi_{0,t}^\nu \cdot I$  for  $0 \leq t \leq 1$ , where  $\phi_{0,t}^\nu$  solves ODE (13). Then (22) equals to*

$$\begin{aligned} \min_{\substack{f(0, \cdot) \in \mathcal{X} \\ \nu \in \mathcal{L}_\gamma^2}} \int_0^1 \left[ \mathcal{D}_{\mathcal{T}_t, g_t}(f(t, \cdot)) + \mu_2 \int_0^t \int_\Omega f(\tau, x) |\nu(\tau, x)|^2 dx d\tau \right] dt + \mu_1 \mathcal{R}_1(f(0, \cdot)) \\ \text{s.t. } \partial_t f(t, \cdot) + \nabla \cdot (f(t, \cdot) \nu(t, \cdot)) = 0. \end{aligned} \quad (23)$$

*Proof.* The proof can be readily obtained by following those of theorem 3 and [16, Theorem 3.5].  $\square$

*Remark 2.* As described in section 2.2, the mass-preserving deformation is required under the principle of optimal transportation. Hence, we merely consider such deformation in theorem 4.

Therefore, the investigation on spatiotemporal imaging can be motivated by the perspective of PDE-constrained optimal control. The other purpose of the PDE-constrained formulation is that it can be simply used to compare against the PDE based alternatives, for instance, the one based on conventional Wasserstein distance in [10]. More details are provided in section 3.3.

## 3.2 Time discretization

The time-discretized version of the proposed model is useful to the practical applications. Without loss of generality, assume that the acquired data is collected at equally discretized time point through the gating method.

We suppose that the sampling is performed on a uniform partition over  $[0, 1]$  with  $\{t_i = i/N\}$  for  $0 \leq i \leq N$ , which acts as the gating grid. Then the time-discretized formulation of the general spatiotemporal imaging in (1) becomes

$$g(t_i, \cdot) = \mathcal{T}_{t_i}(f(t_i, \cdot)) + g_{\text{noise}}(t_i, \cdot). \quad (24)$$

Hence, one of the time discretization of (22) is formulated as

$$\begin{aligned} \min_{\substack{I \in \mathcal{X} \\ \nu \in \mathcal{L}_\gamma^2}} \frac{1}{N} \sum_{i=1}^N \left[ \mathcal{D}_{\mathcal{T}_{t_i}, g_{t_i}}(\phi_{0,t_i}^\nu \cdot I) + \mu_2 \int_0^{t_i} \int_\Omega \phi_{0,\tau}^\nu \cdot I(x) |\nu(\tau, x)|^2 dx d\tau \right] + \mu_1 \mathcal{R}_1(I) \\ \text{s.t. } \phi_{0,t}^\nu \text{ solves ODE (13).} \end{aligned} \quad (25)$$

Actually, using the form (25) means no projection data is acquired at  $t = 0$ . The unknown template acts as a “virtual” image, and merely its warped version  $\phi_{0,t_i}^\nu \cdot I$  relates. The “virtual” image was also considered in [8] for gated PET/CT imaging.

If the projection data is assumed to acquire at  $t = 0$ , then the (22) can be time-discretized as

$$\begin{aligned} \min_{\substack{I \in \mathcal{X} \\ \nu \in \mathcal{L}_\gamma^2}} \frac{1}{N+1} \sum_{i=0}^N \left[ \mathcal{D}_{\mathcal{T}_{t_i}, g_{t_i}}(\phi_{0,t_i}^\nu \cdot I) + \mu_2 \int_0^{t_i} \int_\Omega \phi_{0,\tau}^\nu \cdot I(x) |\nu(\tau, x)|^2 dx d\tau \right] + \mu_1 \mathcal{R}_1(I) \\ \text{s.t. } \phi_{0,t}^\nu \text{ solves ODE (13),} \end{aligned} \quad (26)$$

where the unknown image at the initial gate acts as the template.

To get satisfying result, the template in (26) should be reconstructed as accurate as possible. However, for (25), even if the reconstructed “virtual” template is not so accurate, the velocity field can be used to make correction to obtain the desirable sequential images  $\phi_{0,t}^\nu \cdot I$  ( $1 \leq i \leq N$ ) to some extent. In this article, the time-discretized scheme (25) is adopted to perform numerical implementation.

### 3.3 Comparison with several existing alternatives

In this section, the analytical comparison will be conducted between the proposed model and the existing alternatives.

#### 3.3.1 The joint variational model based on Wasserstein distance

A variational model based on optimal transportation was proposed for joint motion estimation and image reconstruction in [10], which is also based on the  $\mathcal{L}^2$  Wasserstein distance but in different framework. This model is formulated as the following PDE-constrained optimal control problem, which is written as

$$\begin{aligned} \min_{f \geq 0, \nu} \int_0^1 & \left[ \mathcal{D}_{\mathcal{T}_t, g_t}(f(t, \cdot)) + \mu_1 \mathcal{R}_1(f(t, \cdot)) + \mu_2 \int_{\Omega} f(t, x) |\nu(t, x)|^2 dx \right] dt \\ \text{s.t. } & \partial_t f(t, \cdot) + \nabla \cdot (f(t, \cdot) \nu(t, \cdot)) = 0. \end{aligned} \quad (27)$$

It is easy to figure out that the PDE constraints in (23) and (27) are the same. Through analysis, the obvious distinctions between them relate to the constrained space with respect to the velocity field  $\nu$  and the selection of the shape regularization term  $\mathcal{R}_2$ .

As given in (27), the constrained space of velocity fields is  $\mathcal{L}^2([0, 1], \Omega)$ , which leads to the velocity field lacking sufficient smoothness on  $\Omega$ . In contrast to (27), the space of velocity fields in (23) is restricted in  $\mathcal{L}_{\mathcal{V}}^2$ , which means the velocity field at every time point located in an admissible Hilbert space, namely, a sufficiently smooth vector-valued function distributed on  $\Omega$ . This guarantees the non-rigid diffeomorphic deformations, to some extent, which fulfils the physical mechanism [26, 14]. Moreover, the regularization on  $\nu$  in (27) is merely achieved by the  $\mathcal{R}_2(\phi_t)$  at  $t = 1$ . However, the model (23) make use of  $\mathcal{R}_2(\phi_t)$  for all of the time.

Besides those above, both approaches also differ in the selection of regularization term  $\mathcal{R}_1$ . The (23) only poses regularization on the initial image  $f(0, \cdot)$ , whereas in (27) the whole time trajectory  $t \mapsto f(t, \cdot)$  is regularized. Bear in mind that the  $f(t, \cdot)$  is determined by  $f(0, \cdot)$  and  $\nu$ . Hence, (23) not only has a simpler formulation, but also gets the advantage for numerical implementation.

For further comparison, an equivalent result is given by the following theorem if we change the constrained space of velocity fields into  $\mathcal{L}_{\mathcal{V}}^2$  for (27).

**Theorem 5.** *Suppose that the assumptions in theorem 3 hold. Let  $\mathcal{X}$  be a space of nonnegative real-valued functions with appropriate smoothness and compactly supported on  $\Omega$ , and  $f(0, \cdot) \in \mathcal{X}$ , which is denoted by template  $I$ . Then (27) is equivalent to*

$$\begin{aligned} \min_{\substack{I \in \mathcal{X} \\ \nu \in \mathcal{L}_{\mathcal{V}}^2}} \int_0^1 & \left[ \mathcal{D}_{\mathcal{T}_t, g_t}(\phi_{0,t}^\nu \cdot I) + \mu_1 \mathcal{R}_1(\phi_{0,t}^\nu \cdot I) + \mu_2 \int_{\Omega} \phi_{0,t}^\nu \cdot I(x) |\nu(t, x)|^2 dx \right] dt \\ \text{s.t. } & \phi_{0,t}^\nu \text{ solves ODE (13),} \end{aligned} \quad (28)$$

where  $\phi_{0,t}^\nu \cdot I$  is defined as (4).

*Proof.* The proof can be readily obtained by following those of theorem 3 and theorem 4.  $\square$

Let  $\mathcal{E}_W(I, \boldsymbol{\nu})$  be the objective function in (28), and  $\mathcal{V}$  be an RKHS. Following the derivations of the proof in theorem 6, we get the  $\mathcal{L}_{\mathcal{V}}^2$ -gradient with regard to the velocity field  $\boldsymbol{\nu}$  as

$$\begin{aligned} \nabla_{\boldsymbol{\nu}}^{\mathcal{V}} \mathcal{E}_W(I, \boldsymbol{\nu})(t, \cdot) &= \mathcal{K} \left( \phi_{0,t}^{\boldsymbol{\nu}} \cdot I \int_t^1 \nabla \left( \left[ \partial \mathcal{D}_{\tau, g_{\tau}}(\phi_{0,\tau}^{\boldsymbol{\nu}} \cdot I) + \mu_1 \partial \mathcal{R}_1(\phi_{0,\tau}^{\boldsymbol{\nu}} \cdot I) + \mu_2 |\boldsymbol{\nu}(\tau, \cdot)|^2 \right] (\phi_{t,\tau}^{\boldsymbol{\nu}}) \right) d\tau \right. \\ &\quad \left. + 2\mu_2 \phi_{0,t}^{\boldsymbol{\nu}} \cdot I \boldsymbol{\nu}(t, \cdot) \right) \end{aligned} \quad (29)$$

for  $0 \leq t \leq 1$  and the gradient (i.e.,  $\mathcal{L}^2$ -gradient if not indicated) in terms of the template  $I$  as

$$\nabla_I \mathcal{E}_W(I, \boldsymbol{\nu}) = \int_0^1 \left[ \partial \mathcal{D}_{\tau, g_{\tau}}(\phi_{0,t}^{\boldsymbol{\nu}} \cdot I) + \mu_1 \partial \mathcal{R}_1(\phi_{0,t}^{\boldsymbol{\nu}} \cdot I) + \mu_2 |\boldsymbol{\nu}(t, \cdot)|^2 \right] (\phi_{0,t}^{\boldsymbol{\nu}}) dt. \quad (30)$$

Assume that  $(I^*, \boldsymbol{\nu}^*)$  is the solution to the problem (28), which should satisfy the following optimality conditions

$$\begin{cases} \nabla_{\boldsymbol{\nu}}^{\mathcal{V}} \mathcal{E}_W(I^*, \boldsymbol{\nu}^*) = 0, \\ \nabla_I \mathcal{E}_W(I^*, \boldsymbol{\nu}^*) - \lambda^* = 0, \\ \lambda^* \geq 0, \quad I^* \geq 0, \quad \lambda^* I^* = 0, \end{cases} \quad (31)$$

where  $\lambda^*$  is the function of Lagrange multiplier.

In particular, we consider the optimal velocity field at the end points  $t = 0$  and  $t = 1$ . If  $t = 0$  and 1, using (29)–(31), and considering the symmetric and positive-definite reproducing kernel, then we have

$$I^* \boldsymbol{\nu}^*(0, \cdot) = 0 \quad \text{and} \quad \phi_{0,1}^{\boldsymbol{\nu}^*} \cdot I^* \boldsymbol{\nu}^*(1, \cdot) = 0.$$

Hence  $\boldsymbol{\nu}^*(0, \cdot)$  and  $\boldsymbol{\nu}^*(1, \cdot)$  are vanishing on the supports of  $I^*$  and  $\phi_{0,1}^{\boldsymbol{\nu}^*} \cdot I^*$  respectively. Namely, the optimal velocity field that minimizes (28) is vanishing on the supports of the associated images to be reconstructed at the end time points.

On the other hand, suppose that  $(\bar{I}, \bar{\boldsymbol{\nu}})$  is the solution to the problem (22), combined with theorem 6, which fulfils the following optimality conditions

$$\begin{cases} \nabla_{\boldsymbol{\nu}}^{\mathcal{V}} \mathcal{E}_C(\bar{I}, \bar{\boldsymbol{\nu}}) = 0, \\ \nabla_I \mathcal{E}_C(\bar{I}, \bar{\boldsymbol{\nu}}) - \bar{\lambda} = 0, \\ \bar{\lambda} \geq 0, \quad \bar{I} \geq 0, \quad \bar{\lambda} \bar{I} = 0, \end{cases} \quad (32)$$

where  $\bar{\lambda}$  is the associated Lagrange multiplier function. Using (32) and theorem 6, we immediately observe that the optimal velocity field that minimizes (22) is unnecessarily vanishing on the supports of the reconstructed images at the end time points. Following theorem 7, the optimal velocity field to the related time-discretized model is also unnecessarily vanishing at the same domains as the above. This statement has been also demonstrated numerically by the computed optimal velocity field in fig. 4. Hence, this implies the consistency between the time-continuous model and its associated time-discretized counterpart.

### 3.3.2 The joint variational model based on LDDMM

We then recall the LDDMM based model for joint image reconstruction and motion estimation in [16], which implies an LDDMM consistent growth model. Using the same notation, that model with mass-preserving deformation in the form of PDE-constrained optimal control can be written as

$$\begin{aligned} \min_{\substack{f(0, \cdot) \in \mathcal{X} \\ \nu \in \mathcal{L}_V^2}} \int_0^1 \left[ \mathcal{D}_{\mathcal{T}_t, g_t}(f(t, \cdot)) + \mu_2 \int_0^t \int_{\Omega} |L\nu(\tau, x)|^2 dx d\tau \right] dt + \mu_1 \mathcal{R}_1(f(0, \cdot)) \\ \text{s.t. } \partial_t f(t, \cdot) + \nabla \cdot (f(t, \cdot) \nu(t, \cdot)) = 0. \end{aligned} \quad (33)$$

It is obvious that both (23) and (33) constrain the velocity field into the  $\mathcal{L}_V^2$  space. However, the difference is situated on the choice of shape regularization  $\mathcal{R}_2(\phi_t)$  for  $0 \leq t \leq 1$ . Under the framework of shape theory, in (33) the squared shape distance acts as the shape regularization term (see [16]). No any weight is involved or all of the involved weight values are one. It would make sense if the deformation, for instance the geometric deformation, merely moves the position of the pixel/voxel but does not change its intensity.

As stated in section 2.1, the mass-preserving non-rigid deformation not only moves the position of the pixel/voxel but also changes its intensity. In contrast, the proposed model uses the squared  $\mathcal{L}^2$  Wasserstein distance. Particularly, a time-dependent weight function is introduced into the new shape regularization term under the framework of optimal transportation, which is chosen as the unknown time-series image/density  $f(t, \cdot)$ . In other words, the weight is the nonnegative density  $f(t, \cdot)$ , which is positive on the support of  $f(t, \cdot)$ , otherwise is zero. This implies the penalty is only put on the range of the objects in the image, which equivalently means the transportation cost is just originated from the sites having the objects to be transported.

This also demonstrates that the proposed model using diffeomorphic optimal transport combines the thoughts of LDDMM and optimal transportation. Specially, the other alternative is further constructed in section 6.1. Through analyzing these models, the relationship between LDDMM and optimal transportation would be more clear.

## 4 Numerical implementation

To validate the proposed model, we consider a specific example using the time-discretized model (25). The detailed numerical implementation will be presented.

### 4.1 A specific example

As a specific example in CT, the data fidelity term is usually constructed as the squared  $\mathcal{L}^2$ -norm, and the spatial regularization is often selected as the total variation (TV) functional. More clearly,

$$\mathcal{D}_{\mathcal{T}_{t_i}, g_{t_i}}(\phi_{0, t_i}^\nu \cdot I) := \|\mathcal{T}_{t_i}(\phi_{0, t_i}^\nu \cdot I) - g(t_i, \cdot)\|_2^2, \quad (34)$$

$$\mathcal{R}_1(I) := \|\nabla I\|_1, \quad (35)$$

then (25) is specified by

$$\min_{\substack{I \in \mathcal{X} \\ \nu \in \mathcal{L}_V^2}} \frac{1}{N} \sum_{i=1}^N \left[ \|\mathcal{T}_{t_i}(\phi_{0, t_i}^\nu \cdot I) - g(t_i, \cdot)\|_2^2 + \mu_2 \int_0^{t_i} \int_{\Omega} \phi_{0, \tau}^\nu \cdot I(x) |\nu(\tau, x)|^2 dx d\tau \right] + \mu_1 \|\nabla I\|_1 \quad (36)$$

s.t.  $\phi_{0, t}^\nu$  solves ODE (13).

Here the mass-preserving deformation is applied as mentioned previously, i.e.,

$$\phi_{0,t}^{\nu} \cdot I := |D(\phi_{t,0}^{\nu})| I \circ \phi_{t,0}^{\nu},$$

and  $\mathcal{X}$  is assumed to be the nonnegative  $BV(\Omega)$ .

Remark that the proposed model serves as a general model to deal with the motion compensated image reconstruction in various imaging modalities in spatiotemporal setting. One would select the required data fidelity and spatial regularization for different imaging modalities. The following algorithm also can be presented in the general scheme.

We apply the alternating minimization algorithm to solve the model (36) for the involved variables being mutually coupled. More specifically, fixed the velocity field  $\nu$ , the flow of diffeomorphisms  $\phi_{0,t}^{\nu}$  is generated by the ODE (13). Then, the original problem (36) boils down to the following modified static image reconstruction problem

$$\min_{I \in \mathcal{X}} \frac{1}{N} \sum_{i=1}^N \left[ \|\mathcal{T}_{t_i}(\phi_{0,t_i}^{\nu} \cdot I) - g(t_i, \cdot)\|_2^2 + \mu_2 \int_0^{t_i} \int_{\Omega} \phi_{0,\tau}^{\nu} \cdot I(x) |\nu(\tau, x)|^2 dx d\tau \right] + \mu_1 \|\nabla I\|_1. \quad (37)$$

In contrast, given the template  $I$ , then original problem (36) reduces to a sequentially indirect image registration, where we estimate the velocity field  $\nu$  from the time-series data that are indirect observations of the target by

$$\begin{aligned} \min_{\nu \in \mathcal{L}_Y^2} \frac{1}{N} \sum_{i=1}^N \left[ \|\mathcal{T}_{t_i}(\phi_{0,t_i}^{\nu} \cdot I) - g(t_i, \cdot)\|_2^2 + \mu_2 \int_0^{t_i} \int_{\Omega} \phi_{0,\tau}^{\nu} \cdot I(x) |\nu(\tau, x)|^2 dx d\tau \right] \\ \text{s.t. } \phi_{0,t}^{\nu} \text{ solves ODE (13)}. \end{aligned} \quad (38)$$

Let  $\mathcal{E}_{\nu}: \mathcal{X} \rightarrow \mathbb{R}$  and  $\mathcal{E}_I: \mathcal{L}_Y^2 \rightarrow \mathbb{R}$  be the objective functionals in (37) and (38), respectively. We figure out (36) by solving for (37) and (38) alternately, i.e.,

$$\begin{cases} I^{k+1} := \text{the solution to (37) with fixed } \nu = \nu^k, \\ \nu^{k+1} := \text{the solution to (38) with fixed } I = I^{k+1}, \end{cases} \quad (39)$$

or by the scheme via changing the updating order in (39).

## 4.2 Template reconstruction

In what follows we construct the algorithm for template reconstruction by solving the static image reconstruction problem in (37).

The subproblem in (37) is a nonsmooth minimization. We modify the nonsmooth TV term into the smooth one as

$$\|\nabla I\|_1 \approx \int_{\Omega} |\nabla I(x)|_{2,\epsilon} dx := \int_{\Omega} \left( \sum_i (\partial_i I(x))^2 + \epsilon \right)^{1/2} dx, \quad (40)$$

where  $\epsilon > 0$  is sufficiently small, e.g.,  $\epsilon = 10^{-12}$ . This also implies that we reconsider a smoothed model of (36) by the modification above, which is a often used smoothed strategy for TV regularization in image reconstruction.

Then using theorem 7, the smoothed version of (37) can be solved by the following projected gradient descent scheme:

$$I^{k+1} = \text{Proj}_{\geq 0} \left\{ I^k - \alpha^k \nabla \mathcal{E}_{\nu}(I^k) \right\}, \quad (41)$$

where

$$\nabla \mathcal{E}_\nu(I) = \frac{1}{N} \sum_{i=1}^N \left( h_{0,t_i}^{I,\nu} + \mu_2 \eta_{0,t_i}^\nu \right) + \mu_1 \nabla^* \left( \frac{\nabla I}{|\nabla I|_{2,\epsilon}} \right).$$

Here  $\text{Proj}_{\geq 0}$  means the projection operator onto the space with nonnegativity, and  $\alpha^k$  the stepsize for the  $k$ -th iteration. Furthermore, by (34), and (74), (75), for  $t_i \geq t$ , we have

$$h_{t,t_i}^{I,\nu} = 2\mathcal{T}_{t_i}^* (\mathcal{T}_{t_i}(\phi_{0,t_i}^\nu \cdot I) - g(t_i, \cdot))(\phi_{t,t_i}^\nu), \quad (42)$$

$$\eta_{t,t_i}^\nu = \int_t^{t_i} |\nu(t, \cdot)|^2 (\phi_{t,t}^\nu) d\ell, \quad (43)$$

where  $\mathcal{T}$  is assumed to be linear, and  $\mathcal{T}^*$  denotes its adjoint operator. The numerical implementation for the scheme (41) is given in algorithm 1.

For solving the nonsmooth problem above, the convex optimization techniques can be applied but need to introduce more auxiliary variables and parameters than the above algorithm. As did in [16], to optimize the whole problem (36) efficiently, we still employ the iterative scheme (41) to solve the subproblem.

### 4.3 Velocity field estimation

Here we present an algorithm for solving the sequentially indirect image registration (38). To guarantee the velocity field constrained in  $\mathcal{L}_\nu^2$ , and then resulting a flow of diffeomorphisms through ODE (13), we use the gradient descent scheme based on  $\mathcal{L}_\nu^2$ -gradient. By theorem 7, the scheme is written as

$$\nu^{k+1} = \nu^k - \beta^k \nabla^{\mathcal{V}} \mathcal{E}_I(\nu^k), \quad (44)$$

where

$$\nabla^{\mathcal{V}} \mathcal{E}_I(\nu)(t, \cdot) = \frac{1}{N} \sum_{\{i \geq 1: t_i \geq t\}} \mathcal{K} \left( \phi_{0,t}^\nu \cdot I \left[ \nabla (h_{t,t_i}^{I,\nu} + \mu_2 \eta_{t,t_i}^\nu) + 2\mu_2 \nu_{t,t_i} \right] \right),$$

and  $\beta^k$  is the stepsize in the  $k$ -th iteration, by (76), for  $t_i \geq t$ ,

$$\nu_{t,t_i} = \nu(t, \cdot). \quad (45)$$

Here  $h_{t,t_i}^{I,\nu}$  and  $\eta_{t,t_i}^\nu$  are defined by (42) and (43), respectively. The detailed implementation for the scheme (44) is given in algorithm 2.

As indicated in remark 1, here we use the RKHS with a symmetric and positive-definite Gaussian kernel  $\mathcal{K}: \Omega \times \Omega \rightarrow \mathbb{M}_+^{n \times n}$ , for instance defined by (58) for  $n = 2$ , and then the operator  $\mathcal{K}: \mathcal{L}^2(\Omega, \mathbb{R}^n) \rightarrow \mathcal{V}$  is uniquely defined by

$$\langle \nu, \eta \rangle_{\mathcal{L}^2} = \langle \mathcal{K}(\nu), \eta \rangle_{\mathcal{V}},$$

where  $\mathcal{K}(\nu) = \int_{\Omega} \mathcal{K}(\cdot, y) \nu(y) dy$ .

As a result, the sequence  $\{\nu^k\}$  generated by (44) locate in  $\mathcal{L}_\nu^2$  if the initial value of velocity field is selected in the same space, say the given zero velocity field, which ultimately leads to the cluster points located in  $\mathcal{L}_\nu^2$ , and further produces the flow of diffeomorphisms through ODE (13). In contrast, if one uses the  $\mathcal{L}^2$ -gradient descent scheme in (44), the resulting sequence and its cluster points would locate in  $\mathcal{L}^2([0, 1], \Omega)$  instead. This cannot generate a flow of diffeomorphisms for lacking sufficient smoothness. Since the proposed model is nonconvex with regard to the velocity field, the different solving scheme would lead to the different local minimum (see the numerical comparison in test suite 1 of section 5.1.1).

#### 4.4 Numerical discretization

The period  $[0, 1]$  is discretized uniformly into  $MN$  partitions. Then a discretized time grid is formulated as  $\{\tau_j = j/(MN)\}$  for  $j = 0, 1, \dots, MN$ . Hence,  $\tau_{iM} = t_i$  for  $i = 0, 1, \dots, N$ . In other words, each partition  $[t_i, t_{i+1}]$  is subdivided into  $M$  even segments. Evidently, we have  $\tau_i = t_i$  when  $M = 1$ , which means the discretized time grid is consistent with the gating grid. The  $M$  is called the factor of discretized time degree, which determines the fineness of the grid along the temporal axis.

Solving the ODE (13) numerically, the deformations  $\phi_{\tau_i, \tau_{i-1}}^\nu$  and  $\phi_{\tau_i, \tau_{i+1}}^\nu$  can be computed by

$$\phi_{\tau_j, \tau_{j-1}}^\nu \approx \text{Id} - \frac{1}{MN} \nu(\tau_j, \cdot), \quad (46)$$

and

$$\phi_{\tau_j, \tau_{j+1}}^\nu \approx \text{Id} + \frac{1}{MN} \nu(\tau_j, \cdot). \quad (47)$$

By (17) and (46), we have

$$\phi_{\tau_j, 0}^\nu \approx \phi_{\tau_{j-1}, 0}^\nu \circ \left( \text{Id} - \frac{1}{MN} \nu(\tau_j, \cdot) \right) \quad (48)$$

for  $j = 1, 2, \dots, MN$ . Similarly, combining (17) and (47), we obtain the following formula

$$\phi_{\tau_j, t_i}^\nu \approx \phi_{\tau_{j+1}, t_i}^\nu \circ \left( \text{Id} + \frac{1}{MN} \nu(\tau_j, \cdot) \right) \quad (49)$$

for  $j = iM - 1, iM - 2, \dots, 0$ , where  $\phi_{t_i, t_i}^\nu = \text{Id}$ .

Then using (48), the Jacobian determinant can be calculated by

$$|D(\phi_{\tau_j, 0}^\nu)| \approx \left( 1 - \frac{1}{MN} \text{div} \nu(\tau_j, \cdot) \right) |D(\phi_{\tau_{j-1}, 0}^\nu)| \circ \left( \text{Id} - \frac{1}{MN} \nu(\tau_j, \cdot) \right) \quad (50)$$

for  $j = 1, 2, \dots, MN$ . Here  $\phi_{0,0}^\nu = \text{Id}$  and  $|D(\phi_{0,0}^\nu)| = 1$ .

As given in (41), updating the template requires to compute the mass-preserving deformations like  $\phi_{0, t_i}^\nu \cdot I = |D(\phi_{t_i, 0}^\nu)| I \circ \phi_{t_i, 0}^\nu$ .

By (48), we have the following estimate

$$I \circ \phi_{\tau_j, 0}^\nu \approx (I \circ \phi_{\tau_{j-1}, 0}^\nu) \circ \left( \text{Id} - \frac{1}{MN} \nu(\tau_j, \cdot) \right) \quad (51)$$

for  $j = 1, 2, \dots, MN$ , and  $I \circ \phi_{0,0}^\nu = I$ . Multiplying (51) with (50), we have the significant update

$$\phi_{0, \tau_j}^\nu \cdot I \approx \left( 1 - \frac{1}{MN} \text{div} \nu(\tau_j, \cdot) \right) (\phi_{0, \tau_{j-1}}^\nu \cdot I) \circ \left( \text{Id} - \frac{1}{MN} \nu(\tau_j, \cdot) \right). \quad (52)$$

Then for (42), the (49) also yields the following approximation

$$h_{\tau_j, t_i}^{I, \nu} \approx h_{\tau_{j+1}, t_i}^{I, \nu} \circ \left( \text{Id} + \frac{1}{MN} \nu(\tau_j, \cdot) \right) \quad (53)$$

for  $j = iM - 1, iM - 2, \dots, 0$ , where, by (42),

$$h_{t_i, t_i}^{I, \nu} = 2\mathcal{T}_{t_i}^*(\mathcal{T}_{t_i}(\phi_{0, t_i}^\nu \cdot I) - g(t_i, \cdot)).$$

As observed from (41) and (44), we need to discretize  $\eta_{\tau_j, t_i}^\nu$  for  $j = iM - 1, iM - 2, \dots, 0$  and  $i = 1, \dots, N$ . By (43) we know the fact  $\eta_{t_i, t_i}^\nu = 0$  and

$$\eta_{\tau_j, t_i}^\nu = \int_{\tau_j}^{t_i} |\nu(\cdot, \cdot)|^2(\phi_{\tau_j, t}^\nu) dt. \quad (54)$$

We discretize the right-hand side of (54) by

$$\eta_{\tau_j, t_i}^\nu \approx \frac{1}{iM - j} \sum_{l=j+1}^{iM} |\nu(\tau_l, \cdot)|^2(\phi_{\tau_j, \tau_l}^\nu). \quad (55)$$

*Remark 3.* The following scheme

$$\eta_{\tau_j, t_i}^\nu \approx \frac{1}{iM - j + 1} \sum_{l=j}^{iM} |\nu(\tau_l, \cdot)|^2(\phi_{\tau_j, \tau_l}^\nu) \quad (56)$$

is an alternative for discretizing (54). But it has no remarkable improvement to the ultimate result.

Similarly, using (49), we implement the deformation  $\phi_{\tau_j, \tau_l}^\nu$  in (55) by

$$|\nu(\tau_l, \cdot)|^2 \circ \phi_{\tau_s, \tau_l}^\nu \approx |\nu(\tau_l, \cdot)|^2 \circ \phi_{\tau_{s+1}, \tau_l}^\nu \circ \left( \text{Id} + \frac{1}{MN} \nu(\tau_s, \cdot) \right) \quad (57)$$

for  $s = l - 1, l - 2, \dots, j$ .

## 4.5 Algorithms

As analyzed in section 4.1, we need to solve (36) by the alternating iterative scheme in (39). At each iteration two subproblems will be solved, namely, updating  $I$  with given  $\nu$  (algorithm 1) and updating  $\nu$  with given  $I$  (algorithm 2).

### 4.5.1 Algorithm for template reconstruction

Using the discretization in section 4.4, we give detailed implementation of the projected gradient descent scheme in algorithm 1 for minimizing the smoothed version of (37) as described in section 4.2.

### 4.5.2 Algorithm for velocity field estimation

Here we list the numerical implementation of gradient descent scheme for velocity field estimation in section 4.3. The following algorithm 2 outlines the procedure for computing the scheme (44) that makes use of the discretization in section 4.4.

### 4.5.3 Alternating minimization algorithm

Ultimately, the alternating minimization algorithm for recovering the template and velocity field is presented in the following algorithm 3. The iteration number for solving each inner subproblem is restricted to be one. The complexity of the algorithm is comparable to the counterpart in [16].

**Algorithm 1** Projected gradient descent (41) for template reconstruction

1: *Initialize:* Let  $t_i \leftarrow \frac{i}{N}$  for  $i = 0, \dots, N$ ,  $\tau_j \leftarrow \frac{j}{MN}$  for  $j = 0, \dots, MN$ . Given initial template  $I^0$ , velocity field  $\nu$ , regularization parameters  $\mu_1 > 0$  and  $\mu_2 > 0$ , error tolerance  $\epsilon_I > 0$ , stepsize  $\alpha > 0$ , and iteration number  $K_I > 0$ . Let  $k \leftarrow 0$ .

2: *Loop:*

3: Compute  $\phi_{0,\tau_j}^\nu \cdot I^k$  by (52):

$$\phi_{0,\tau_j}^\nu \cdot I^k \leftarrow \left(1 - \frac{1}{MN} \operatorname{div} \nu(\tau_j, \cdot)\right) (\phi_{0,\tau_{j-1}}^\nu \cdot I^k) \circ \left(\operatorname{Id} - \frac{1}{MN} \nu(\tau_j, \cdot)\right)$$

for  $1 \leq j \leq MN$ , where  $\phi_{0,0}^\nu \cdot I^k = I^k$ .

4: Estimate  $h_{0,t_i}^{I^k, \nu}$  for  $1 \leq i \leq N$  by (53):

$$h_{\tau_j, t_i}^{I^k, \nu} \leftarrow h_{\tau_{j+1}, t_i}^{I^k, \nu} \circ \left(\operatorname{Id} + \frac{1}{MN} \nu(\tau_j, \cdot)\right)$$

for  $j = iM - 1, iM - 2, \dots, 0$ , and update  $h_{t_i, t_i}^{I^k, \nu}$  by

$$h_{t_i, t_i}^{I^k, \nu} \leftarrow 2\mathcal{T}_{t_i}^*(\mathcal{T}_{t_i}(\phi_{0,t_i}^\nu \cdot I^k) - g(t_i, \cdot)).$$

5: Compute  $\eta_{0,t_i}^\nu$  for  $1 \leq i \leq N$  by (55):

$$\eta_{0,t_i}^\nu \leftarrow \frac{1}{iM} \sum_{l=1}^{iM} |\nu(\tau_l, \cdot)|^2 (\phi_{0,\tau_l}^\nu),$$

where for  $1 \leq l \leq iM$ , by (57),

$$|\nu(\tau_l, \cdot)|^2 \circ \phi_{\tau_s, \tau_l}^\nu \leftarrow |\nu(\tau_l, \cdot)|^2 \circ \phi_{\tau_{s+1}, \tau_l}^\nu \circ \left(\operatorname{Id} + \frac{1}{MN} \nu(\tau_s, \cdot)\right)$$

for  $s = l - 1, l - 2, \dots, 0$ .

6: Update  $\nabla \mathcal{E}_\nu(I^k)$  by

$$\nabla \mathcal{E}_\nu(I^k) \leftarrow \frac{1}{N} \sum_{i=1}^N \left(h_{0,t_i}^{I^k, \nu} + \mu_2 \eta_{0,t_i}^\nu\right) + \mu_1 \nabla^* \left(\frac{\nabla I^k}{|\nabla I^k|_{2,\epsilon}}\right).$$

7: Evaluate  $I^{k+1}$  by

$$I^{k+1} \leftarrow \operatorname{Proj}_{\geq 0} \left\{ I^k - \alpha \nabla \mathcal{E}_\nu(I^k) \right\}.$$

8: **If**  $|I^{k+1} - I^k| > \epsilon_I$  and  $k < K_I$ , then  $k \leftarrow k + 1$ , **goto** *Loop*.

9: **Output**  $I^{k+1}$ .

**Algorithm 2** Gradient descent (44) for velocity field estimation

1: *Initialize*: Let  $t_i \leftarrow \frac{i}{N}$  for  $i = 0, \dots, N$ ,  $\tau_j \leftarrow \frac{j}{MN}$  for  $j = 0, \dots, MN$ . Given initial velocity field  $\boldsymbol{\nu}^0(\tau_j)$ , template  $I$ , regularization parameter  $\mu_2 > 0$ , error tolerance  $\epsilon_\nu > 0$ , stepsize  $\beta > 0$ , and iteration number  $K_\nu > 0$ . Fixed kernel function  $\mathcal{K}(\cdot, \cdot)$ . Let  $k \leftarrow 0$ .

2: *Loop*:

3: Compute  $\phi_{0,\tau_j}^{\boldsymbol{\nu}^k} \cdot I$  by (52):

$$\phi_{0,\tau_j}^{\boldsymbol{\nu}^k} \cdot I \leftarrow \left(1 - \frac{1}{MN} \operatorname{div} \boldsymbol{\nu}^k(\tau_j, \cdot)\right) (\phi_{0,\tau_{j-1}}^{\boldsymbol{\nu}^k} \cdot I) \circ \left(\operatorname{Id} - \frac{1}{MN} \boldsymbol{\nu}^k(\tau_j, \cdot)\right)$$

for  $1 \leq j \leq MN$ , where  $\phi_{0,0}^{\boldsymbol{\nu}^k} \cdot I = I$ .

4: Update  $h_{\tau_j, t_i}^{I, \boldsymbol{\nu}^k}$  for  $1 \leq i \leq N$  by (53):

$$h_{\tau_j, t_i}^{I, \boldsymbol{\nu}^k} \leftarrow h_{\tau_{j+1}, t_i}^{I, \boldsymbol{\nu}^k} \circ \left(\operatorname{Id} + \frac{1}{MN} \boldsymbol{\nu}^k(\tau_j, \cdot)\right)$$

for  $j = iM - 1, iM - 2, \dots, 0$  and compute  $h_{t_i, t_i}^{I, \boldsymbol{\nu}^k}$  for  $1 \leq i \leq N$  by

$$h_{t_i, t_i}^{I, \boldsymbol{\nu}^k} \leftarrow 2\mathcal{T}_{t_i}^* (\mathcal{T}_{t_i}(\phi_{0, t_i}^{\boldsymbol{\nu}^k} \cdot I) - g(t_i, \cdot)).$$

5: Compute  $\eta_{\tau_j, t_i}^{\boldsymbol{\nu}^k}$  for  $1 \leq i \leq N$  by (55):

$$\eta_{\tau_j, t_i}^{\boldsymbol{\nu}^k} \leftarrow \frac{1}{iM - j} \sum_{l=j+1}^{iM} |\boldsymbol{\nu}^k(\tau_l, \cdot)|^2 (\phi_{\tau_j, \tau_l}^{\boldsymbol{\nu}^k}),$$

where for  $j < l \leq iM$ , by (57),

$$|\boldsymbol{\nu}^k(\tau_l, \cdot)|^2 \circ \phi_{\tau_s, \tau_l}^{\boldsymbol{\nu}^k} \leftarrow |\boldsymbol{\nu}^k(\tau_l, \cdot)|^2 \circ \phi_{\tau_{s+1}, \tau_l}^{\boldsymbol{\nu}^k} \circ \left(\operatorname{Id} + \frac{1}{MN} \boldsymbol{\nu}^k(\tau_s, \cdot)\right)$$

for  $s = l - 1, l - 2, \dots, j$ .

6: Evaluate  $\nabla^{\mathcal{Y}} \mathcal{E}_I(\boldsymbol{\nu}^k)(\tau_j, \cdot)$  (using fast Fourier transform to compute the convolution) by

$$\nabla^{\mathcal{Y}} \mathcal{E}_I(\boldsymbol{\nu}^k)(\tau_j, \cdot) \leftarrow \frac{1}{N} \sum_{\{i \geq 1: t_i \geq \tau_j\}} \mathcal{K} \left( \phi_{0, \tau_j}^{\boldsymbol{\nu}^k} \cdot I \left[ \nabla (h_{\tau_j, t_i}^{I, \boldsymbol{\nu}^k} + \mu_2 \eta_{\tau_j, t_i}^{\boldsymbol{\nu}^k}) + 2\mu_2 \boldsymbol{\nu}_{\tau_j, t_i}^k \right] \right)$$

for  $0 \leq j \leq MN$ .

7: Update  $\boldsymbol{\nu}^k(\tau_j, \cdot)$  for  $0 \leq j \leq MN$  by:

$$\boldsymbol{\nu}^{k+1}(\tau_j, \cdot) \leftarrow \boldsymbol{\nu}^k(\tau_j, \cdot) - \beta \nabla^{\mathcal{Y}} \mathcal{E}_I(\boldsymbol{\nu}^k)(\tau_j, \cdot).$$

8: **If**  $|\boldsymbol{\nu}^{k+1} - \boldsymbol{\nu}^k| > \epsilon_\nu$  and  $k < K_\nu$ , then  $k \leftarrow k + 1$ , **goto** *Loop*.

9: **Output**  $\boldsymbol{\nu}^{k+1}$ .

**Algorithm 3** Alternating minimization algorithm

- 
- 1: *Initialize*: Given  $M, N$ . Let  $t_i \leftarrow \frac{i}{N}$  for  $i = 0, \dots, N$ ,  $\tau_j \leftarrow \frac{j}{MN}$  for  $j = 0, \dots, MN$ . Given initial velocity field  $\nu^0$  and template  $I^0$ , regularization parameters  $\mu_1 > 0$  and  $\mu_2 > 0$ , error tolerances  $\epsilon_I > 0$  and  $\epsilon_\nu > 0$ , fixed stepsizes  $\alpha^k = \alpha > 0$  and  $\beta^k = \beta > 0$ , and maximum iteration number  $K > 0$ . Fixed kernel function  $K(\cdot, \cdot)$ . Let  $k \leftarrow 0$ .
  - 2: *Loop*:
  - 3: Set  $\nu = \nu^k$ . Run steps 3-7 of algorithm 1. Update  $I^{k+1}$ .
  - 4: Set  $I = I^{k+1}$ . Run steps 3-7 of algorithm 2. Update  $\nu^{k+1}$ .
  - 5: **Or**
  - 6: Set  $I = I^k$ . Run Lines 3-7 of algorithm 2. Update  $\nu^{k+1}$ .
  - 7: Set  $\nu = \nu^{k+1}$ . Run Lines 3-7 of algorithm 1. Update  $I^{k+1}$ .
  - 8:
  - 9: **If**  $|\nu^{k+1} - \nu^k| > \epsilon_\nu$  or  $|I^{k+1} - I^k| > \epsilon_I$ , and  $k < K$ ,
  - 10: then  $k \leftarrow k + 1$ , **goto** *Loop*.
  - 11: **Output**  $I^{k+1}, \nu^{k+1}$ .
- 

## 5 Numerical experiments

To evaluate the proposed method, we adopt the very sparse and/or highly noisy data sets simulated in 2D spatial and temporal tomography, which are measured from the mass-preserving sequential images by parallel beam scanning. The implemented algorithms were programmed in Python. The routines were operated on ThinkStation Xeon E5-2620 v4 2.10 GHz CPU, 64GB ROM, TITAN Xp GPU. The GPU was merely used to accelerate the forward and backward projections. The test section illustrates the performance of the proposed method even though this is not a full evaluation. The implementation is partially supported by Operator Discretization Library (<http://github.com/odlgroup/odl>).

The forward operator  $\mathcal{T}_t: \mathcal{X} \rightarrow \mathcal{Y}$  is specified by Radon transform in  $\mathbb{R}^2$ , namely,

$$R(f)(\theta, x) = \int_{\mathbb{R}} f(x + s\theta) ds \quad \text{for } \theta \in S^1 \text{ and } x \in \theta^\perp,$$

where  $R$  represents the Radon transform,  $S^1$  is the unit circle, and  $(\theta, x)$  determines a line through  $x$  in  $\mathbb{R}^2$  with direction  $\theta$ . Additionally, the  $\mathcal{Y}$  denotes the space of vector fields that is specified by an RKHS with the following Gaussian kernel function

$$K(x, y) := \exp\left(-\frac{1}{2\sigma^2}\|x - y\|_2^2\right) \begin{pmatrix} 1 & 0 \\ 0 & 1 \end{pmatrix} \quad \text{for } x, y \in \mathbb{R}^2, \quad (58)$$

where the  $\sigma > 0$  determines the kernel width.

The mass-preserving images of all gates are defined on  $\Omega$ . For the image at each gate, the noise-free data for per view is obtained by the 2D parallel beam projection, which is then added the Gaussian white noise at a certain level resulting in the noisy data. The noise level is quantified by signal-to-noise ratio (SNR) in logarithmic decibel (dB).

### 5.1 Test suites and results

The test suites are dedicated to assessing the performance against the overview evaluation, different noise levels, and the sensitivity against various selections of regularization parameters  $\mu_1, \mu_2$ , and kernel width  $\sigma$ . We also compare the proposed method numerically to the methods by using TV-based reconstruction, and  $\mathcal{L}^2$ -gradient descent scheme.

### 5.1.1 Test suite 1: Overview evaluation

Here we prepare a test for evaluating the overview performance with regard to numerical convergence, reconstructed accuracy, and mass-preserving property. This test uses a multi-object phantom with five gates (i.e.,  $N = 5$ ). The masses of the sequential images are the same. The ground truth at each gate is shown in the last row of fig. 3, which is adapted from [17]. The image at each gate is consisting of six separately star-like objects with grey-values ranging on  $[0, 1]$ , which is digitized by using  $438 \times 438$  pixels. The images of all gates are supported on a fixed rectangular domain  $[-16, 16] \times [-16, 16]$ .

To show the performance of the proposed method, we use the noise-free measurements. For the image at each gate, the noise-free data per view is measured by 2D parallel beam scanning geometry with evenly 620 bins, which is supported on the range of  $[-24, 24]$ . For the gate  $i$  ( $1 \leq i \leq N$ ), the scanning views are distributed on  $[(i-1)\pi/36, \pi + (i-1)\pi/36]$  uniformly, and the total view number is only six.

It is well-known that when the gradient of the image is sparse, tomographic reconstruction by TV-based reconstruction method outperforms other methods, such as filtered back projection (FBP), the iterative methods without considering priori knowledge. This is especially notable when the data is undersampled. In this test, the used phantom has sparse gradient, and the sampling is quite sparse (six views per gate). However, assume that we neglect the dynamic motions among the gates (i.e., disregard any temporal evolution), and just treat the spatiotemporal problem as a static one. Then the whole tomographic data set is equivalently sampled from 30 projection views. We conduct image reconstruction with the TV-based method. The reconstructed image carries severe motion artifacts as illustrated in fig. 1, the distributed intensity of which is also disordered for the mass-preservation among these sequential images. In contrast, the proposed method exclusively focuses on dealing with such spatiotemporal imaging problem, and is applied to reconstruct the dynamically sequential images with mass-preservation.

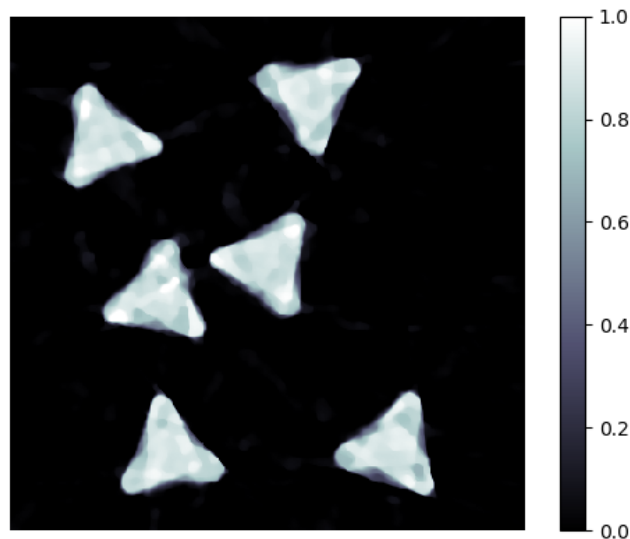


Fig. 1: Test suite 1. Reconstructed image by the TV-based method if the spatiotemporal problem is treated as a static one.

In the proposed model, the regularization parameters  $(\mu_1, \mu_2)$  are selected as  $(0.01, 10^{-7})$  for the noise-free measurements. The factor  $M$  of discretized time degree is set to be 2. The kernel width  $\sigma$  is selected to be 2. The gradient descent stepsizes are fixed as  $\alpha = 0.01$  and  $\beta = 0.05$ , respectively. Firstly we apply algorithm 1 to obtain an initial template image after 50 iterations by using all of the gated data with given zero velocity field. This is actually using static TV-based method to perform 50 iterations. Then we use algorithm 3 to solve the proposed model by the obtained initial template and zero initialized velocity field. Note that the above iteration number is flexible, which just needs enough to gain an appropriately initial template for algorithm 3.

To validate the numerical convergence of the proposed algorithm, we set the maximum iteration number to be sufficiently large, for instance, 2000. The descent curve of the objective functional is plotted in fig. 2, which shows the stable convergence. Additionally, the reconstructed results are shown in the third row of fig. 3. It is clear that the reconstructed image at each gate are almost the same as the corresponding ground truth from visual observation.

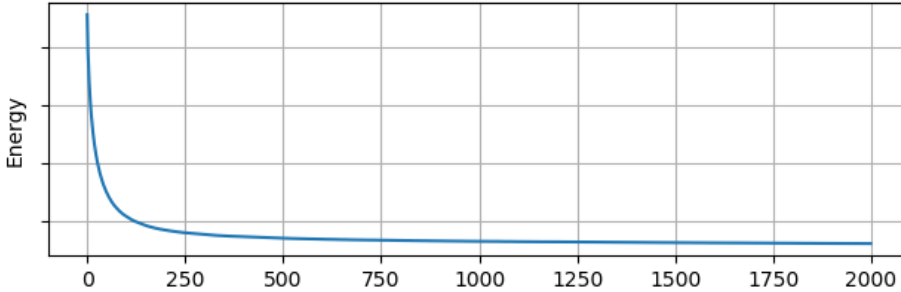


Fig. 2: Test suite 1. Descent curve of the objective functional of the proposed model as the iteration grew.

We also compare the proposed method against some other approaches. In this test, the used phantom (ground truth image) has sparse gradient, and the sampling is sparse (six views per gate), so it is fairly comparing against TV-based reconstruction method. We use the TV-based method to perform reconstruction for the same projection data at each gate. The regularization parameter and the stepsize are chosen as  $\alpha = 0.01$  and  $\lambda = 0.01$  respectively, which are the same as the proposed method. After sufficiently the same 2000 iterations for each gate, the reconstructed results are shown in the first row of fig. 3. It is observed that these reconstructed images have severely stair-like blocks even though the shape structures of the objects are similar to those counterparts in the ground truth.

Moreover, to obtain the diffeomorphic deformations, the velocity field at each time point is restricted into the RKHS  $\mathcal{V}$  in the proposed model. Hence we use the  $\mathcal{L}_{\mathcal{V}}^2$ -gradient descent scheme to solve the optimal velocity field. To validate its necessity, we substitute it by the more general  $\mathcal{L}^2$  space, and then apply the  $\mathcal{L}^2$ -gradient descent scheme to solve the same problem in section 4.3. To make fair comparison, we set the two regularization parameters as the same as the proposed method. Because the iterated velocity field lacks smoothness, the algorithm is not convergent under the same stepsizes as before. So the associated stepsizes are shortened as  $\alpha = 0.001$  and  $\beta = 0.005$ . As a result, a convergent result is obtained as shown in the second row in fig. 3 after sufficiently the 2000 iterations. As we can see, the reconstructed images carry severe artifacts on the objects other than similar shapes as the ground truth. Furthermore, we show their computed optimal velocity fields at the end points in fig. 4. Clearly, the computed

optimal velocity field by the  $\mathcal{L}^2$ -gradient descent scheme is nonsmooth, but that by  $\mathcal{L}^2_\gamma$ -gradient descent scheme is quit smooth as expected.

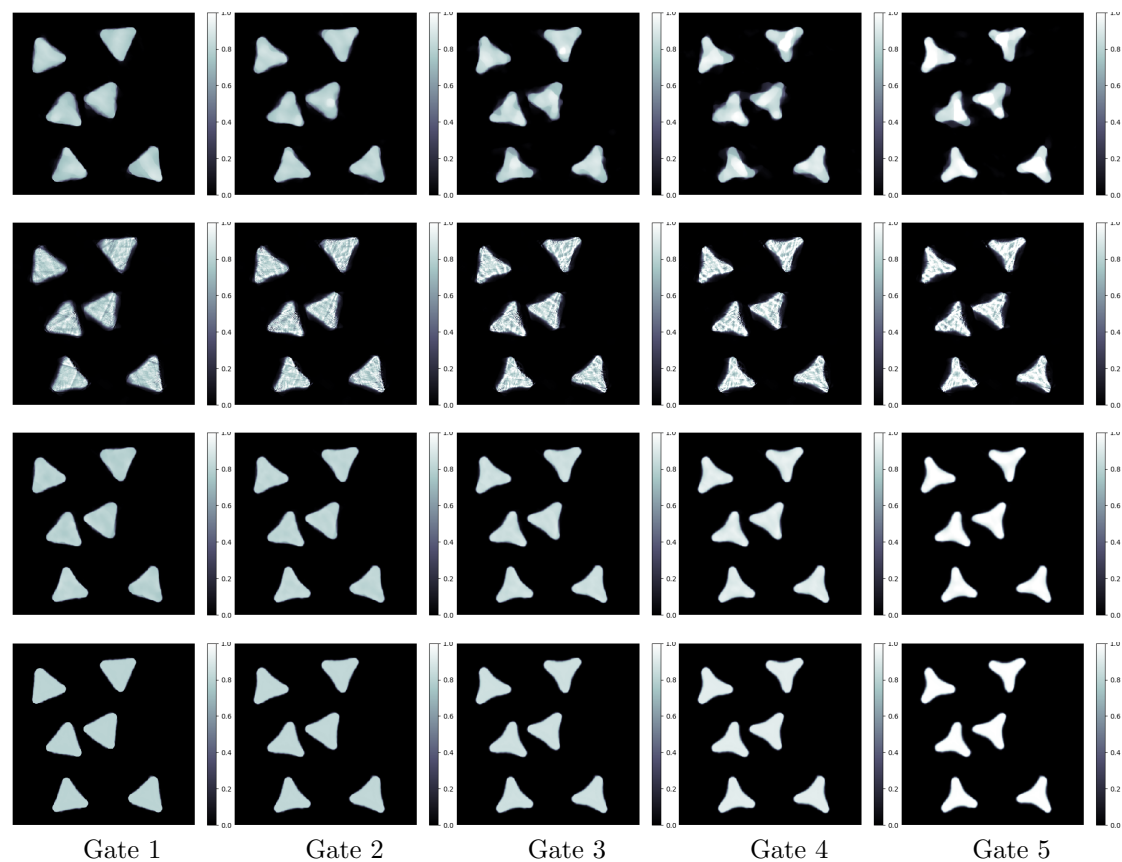


Fig. 3: Test suite 1. Reconstructed images of the multi-object phantom. The columns represent the different gates. For the noise-free data, the first three rows are the reconstructed spatiotemporal images by TV-based reconstruction method (row 1), the algorithm using  $\mathcal{L}^2$ -gradient descent method (row 2), and the proposed method (row 3). The last row (row 4) shows the ground truth for each gate.

Apart from the visual contrast, the reconstruction is quantitatively compared using structural similarity (SSIM), peak signal-to-noise ratio (PSNR) and normorlized root mean-squared error (NRMSE), which is frequently used to evaluate the image quality of reconstruction [57]. The larger of the first two indexes implies the better image quality. But the larger of the last index means the worse image quality. For the reconstruction results of different methods with the same noise-free data, the values of SSIM, PSNR and NRMSE of the reconstructed spatiotemporal images compared to the related ground truths are tabulated in table 1.

As compared these values with each other, the values of SSIM by the proposed method is bigger than those by TV-based method and using  $\mathcal{L}^2$ -gradient descent method. Additionally, the values of PSNR by the proposed method are much bigger than the those by the other two methods. And the values of NRMSE by the proposed method are much smaller than those by the other two methods. The statements are also consistent with the visual observation in fig. 3.

Hence both visual and quantitative comparisons demonstrate that the reconstructed images

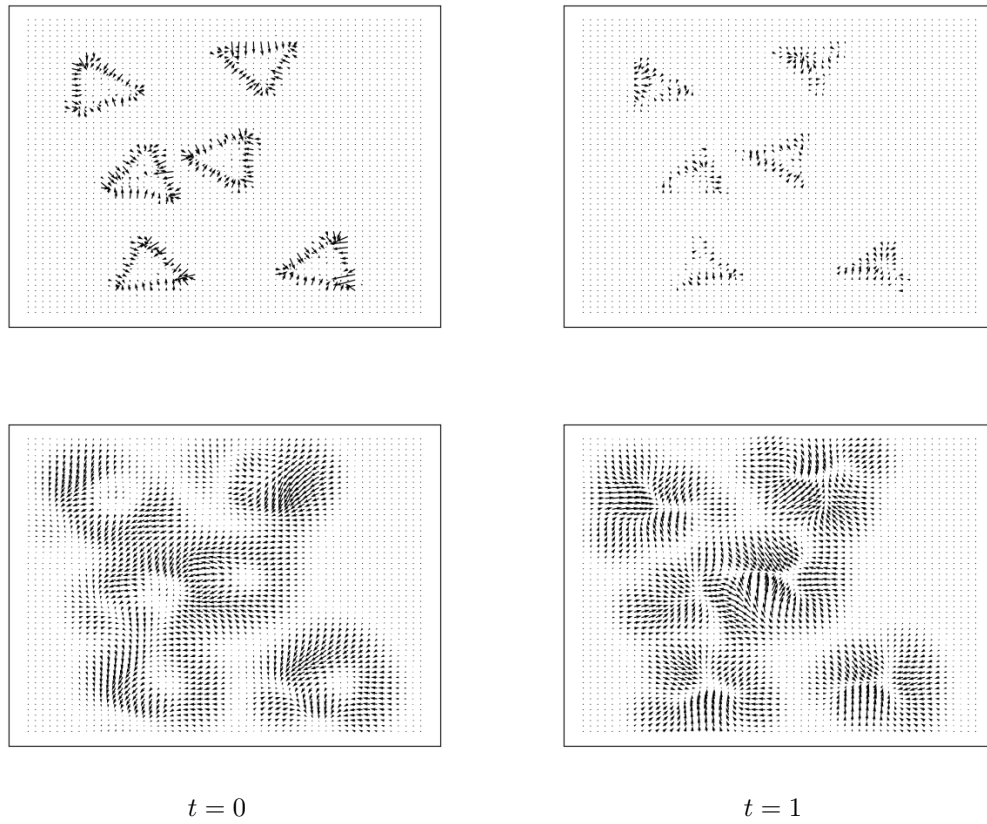


Fig. 4: Test suite 1. The computed optimal velocity field at the end time points  $t = 0$  (left) and  $t = 1$  (right) by the  $\mathcal{L}^2$ -gradient descent scheme (top) and the proposed method (bottom) in fig. 3, respectively.

	Gate 1	Gate 2	Gate 3	Gate 4	Gate 5
TV	0.9571	0.9609	0.9416	0.9279	0.9350
	26.70	28.15	26.58	25.31	27.05
	0.1283	0.1102	0.1355	0.1628	0.1397
$\mathcal{L}^2$ gradient	0.8749	0.8686	0.8650	0.8644	0.8677
	22.36	20.73	20.37	20.65	21.28
	0.2115	0.2591	0.2770	0.2784	0.2716
Proposed	0.9819	0.9879	0.9893	0.9892	0.9874
	31.60	36.20	38.21	38.10	35.83
	0.0729	0.0437	0.0355	0.0373	0.0509

Tab. 1: Test suite 1. The values of SSIM, PSNR and NRMSE of the reconstructed spatiotemporal images compared to the related ground truths for the noise-free measurements, see fig. 3 for reconstructed images. Each table entry has three values that the upper is the value of SSIM, the middle is the value of PSNR, and the bottom is the value of NRMSE, which corresponds to the image at the counterpart position of rows 1–3 in fig. 3.

by the proposed method is much more approximated to the corresponding ground truths. In other words, the proposed method largely improved the quality of the reconstructed images.

Finally, the masses of the reconstructed images are hopefully to be preserved. In order to inspect this characteristic, we obtain all of the masses of the images in fig. 3. As listed in table 2, the values of the mass of ground truths are all 111.75 for that we uses the originally sequential images with the same masses. It is clear in table 2 that the mass of the reconstructed images is preserved very well during the numerical implementation of the proposed method, which is better than the  $\mathcal{L}^2$ -gradient descent method. Moreover, we found that the mass of the result at each gate by the proposed method is almost the same as TV-based method. Since the TV-based reconstruction method is implemented gate by gate, the mass of the result at each gate should be the same essentially. Even though the masses have a little bit errors compared with the ground truths, that is reasonable because these images are reconstructed only from six-angle projection data. Hence, the proposed method has desirable performance on the mass-preserving property.

	Gate 1	Gate 2	Gate 3	Gate 4	Gate 5
TV	112.20	112.21	112.18	112.19	112.21
$\mathcal{L}^2$ gradient	113.83	112.83	111.58	110.92	110.54
Proposed	112.02	112.15	112.22	112.27	112.24
Ground truth	111.75	111.75	111.75	111.75	111.75

Tab. 2: Test suite 1. The values of masses of the reconstructed images, which corresponds to the image at the counterpart position in fig. 3.

### 5.1.2 Test suite 2: Robustness against different noise levels

The images are reconstructed by using the noise-free data in test suite 1. To test the robustness against different noise levels of the proposed method, here the same multi-object phantom is used, and three different levels of additive Gaussian white noise are added onto the above noise-free data. The resulting SNR are about 14.6dB, 7.69dB, and 5.53dB, respectively. To show the noise levels more clear, we profile the noise-free and noisy projection data of the first view of at Gate 1 in fig. 5. To some extent, such three data sets can be seen as the cases of low, moderate and high noise levels correspondingly.

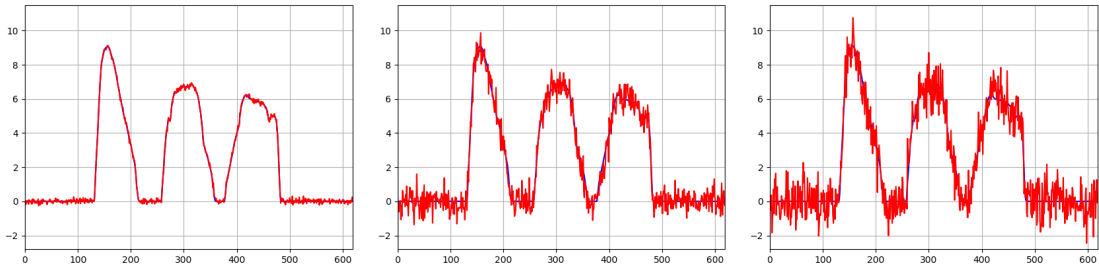


Fig. 5: Test suite 2. Data of the first projection view at Gate 1. The left, middle, and right figures show the data of the first view with 14.6dB, 7.69dB, and 5.53dB noise levels, respectively. The blue curve denotes the noise-free data, and the red jagged curve shows the noisy data.

During numerical implementations, the regularization parameters  $(\mu_1, \mu_2)$  are selected as  $(0.05, 10^{-7})$ ,  $(0.1, 10^{-7})$  and  $(0.15, 10^{-7})$  for the data with 14.6dB, 7.69dB and 5.53dB noise lev-

els, respectively. The lower SNR, the larger value of  $\mu_1$  for the spatio regularization term. The maximum iteration number is set to be 2000 for sufficiently numerical convergence. The associated stepsizes are set as  $\alpha = 0.001$  and  $\beta = 0.005$ . As before, the initial template is obtained by algorithm 1 for 50 iterations using all of the data with given zero velocity field. Then we use algorithm 3 to solve the proposed model with the obtained initial template and zero initialized velocity field. The reconstructed results are shown in fig. 6. It is demonstrated that the reconstructed images by the proposed method (rows 1, 3 and 5) are close to the corresponding ground truth in fig. 3, even though the noise level of the data is higher and higher. Additionally, the image at each single gate is also reconstructed by the TV-based method for numerical comparison, as shown in rows 2, 4 and 6 of fig. 6 for each the same noise level data. Obviously, the reconstructed results by the proposed method is much better than the TV-based method.

Moreover, as we did in test suite 1, the reconstruction results are quantitatively compared by using the indexes of SSIM, PSNR and NRMSE. For the reconstruction results of various methods for different noise level data, the values of SSIM, PSNR and NRMSE of the reconstructed spatiotemporal images compared to the corresponding ground truths are tabulated in table 3.

	Gate 1	Gate 2	Gate 3	Gate 4	Gate 5
Proposed	0.9498	0.9660	0.9699	0.9697	0.9661
	26.47	30.86	32.33	32.43	31.18
	0.1317	0.0807	0.0699	0.0717	0.0869
TV	0.8827	0.8799	0.8548	0.8440	0.8316
	21.68	21.74	20.94	20.09	20.43
	0.2286	0.2307	0.2594	0.2968	0.2994
Proposed	0.9050	0.9239	0.9294	0.9306	0.9295
	24.35	27.24	27.99	28.12	28.06
	0.1681	0.1224	0.1153	0.1177	0.1244
TV	0.8372	0.8431	0.8252	0.7930	0.7933
	20.28	20.48	20.15	19.39	19.70
	0.2685	0.2667	0.2842	0.3217	0.3257
Proposed	0.8564	0.8770	0.8838	0.8861	0.8856
	22.98	25.17	25.62	26.29	26.14
	0.1968	0.1553	0.1515	0.1454	0.1552
TV	0.8086	0.7784	0.7514	0.7521	0.7618
	19.82	19.14	18.78	18.62	19.36
	0.2833	0.3112	0.3327	0.3518	0.3388

Tab. 3: Test suite 2. The values of SSIM, PSNR and NRMSE of the reconstructed spatiotemporal images compared to the related ground truths for the different noise level measurements, see fig. 6 for detailed images. The upper and bottom of each row denote the results obtained by the proposed method and TV-based reconstruction method respectively. Each table entry has three values that the upper is the value of SSIM, the middle is the value of PSNR, and the bottom is the value of NRMSE, which corresponds to the image at the counterpart position in fig. 6.

As listed in table 3, the associated values of SSIM and PSNR obtained by the proposed method is much bigger than TV-based method. And the values of NRMSE by the proposed method are much smaller than those by the TV-based method. These statements are also consistent with the visual observation in fig. 6.

Hence the visual and quantitative comparisons demonstrate that the reconstructed images

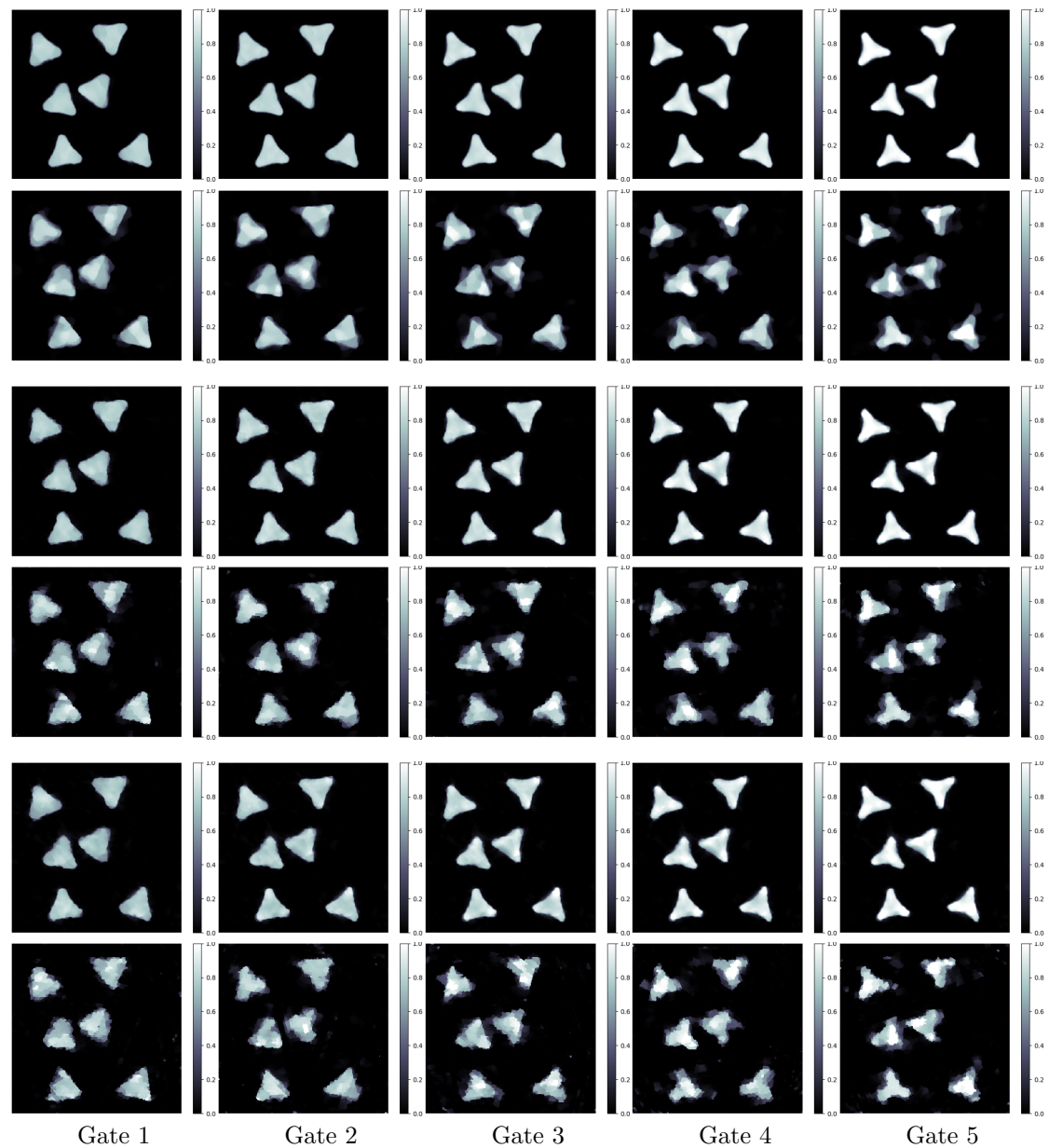


Fig. 6: Test suite 2. Reconstructed spatiotemporal images from the data with different noise levels. The columns represent the different gates. The reconstructed results by the proposed method and TV-based reconstruction method using about 14.6dB data (rows 1 and 2), 7.69dB data (rows 3 and 4), and 5.53dB data (rows 5 and 6), respectively. The ground truth at each gate is displayed in the last row of fig. 3.

by the proposed method is much more approximated to the corresponding ground truths. Even if the projection data is disturbed by different noise levels, the proposed method is able to produce desirable results robustly, which can track the motions of the objects and reconstruct the sequential images accurately.

### 5.1.3 Test suite 3: Sensitivity against selections of regularization parameters

There are three regularization parameters  $\mu_1$ ,  $\mu_2$  and kernel width  $\sigma$  required to select in the proposed model. The meaning of them has been illuminated in the previous sections. Hence the sensitivity test should be concerned against the selection of these parameters.

A heart-like phantom at the first gate is used in this test, which is originated from [27]. To produce the ground truths at the other gates, we take the given mass-preserving deformations against the phantom above. As shown in the last row of fig. 7, the ground truth at each gate is consisting of a heart-like object with different grey-value ranges. These images are digitized using  $120 \times 120$  pixels, and displayed on a fixed rectangular domain  $[-4.5, 4.5] \times [-4.5, 4.5]$ . For the image at each gate, the noise-free data per view is measured by evaluating the 2D parallel beam scanning geometry with uniformly 170 bins, which is defined on the range of  $[-6.4, 6.4]$ . Then the additive Gaussian white noise is added onto the noise-free data. The resulting SNR is about 13dB. For gate  $i$  ( $1 \leq i \leq N$ ), the scanning views are distributed on  $[(i-1)\pi/5, \pi + (i-1)\pi/5]$  evenly, which totally has five views. The factor of discretized time degree is  $M = 8$ . The gradient stepsizes are set as  $\alpha = 0.01$  and  $\beta = 0.05$ , respectively.

Having a good initial template is important to the final result. Using the same method as the previous test suites to get the initial template does not work here. That is because the degree of motions involved in this test is much larger than the previous ones. To this case, it is hard to obtain an applicable initial template by the algorithm 1 with given zero velocity field using all of gated data. So we first employ algorithm 1 to gain an initial template just by the projection data at the first gate by 2000 iterations with the given zero velocity field, which is equivalent to apply the TV-based reconstruction, and then apply algorithm 2 to obtain an initial velocity field by 500 iterations based on the initial template above. Note that the setting of the above iteration numbers is flexible, and the aim is to get good initial template and initial velocity field. Starting from these initialized values, we finally use algorithm 3 to solve the proposed model. By selecting different values for regularization parameters and kernel width, after sufficiently 500 iterations, the reconstructed results are obtained, as shown in rows 2-5 of fig. 7. The detailed selections of varying parameter values can be referred to the caption. For comparison, we also present the reconstructed image at each single gate using TV-based regularization method, as displayed in the first row of fig. 7. As shown in fig. 7, even through we choose different values for these regularization parameters, the corresponding reconstructed results by the proposed method are almost the same, and all close to the counterpart ground truths. However, the reconstructed result by TV-regularization is severely degraded.

Furthermore, the reconstruction results are quantitatively compared to the corresponding ground truths by using SSIM, PSNR and NRMSE. These calculated indexes are listed in table 4. As given in the table, the corresponding SSIM and PSNR indexes of the proposed method are relatively larger than those obtained by TV-based method, and the indexes of NRMSE are smaller. Remark that the obtained indexes by the proposed method are quite similar with each other even if the different parameter pairs are selected.

As visual and quantitative comparisons by fig. 7 and table 4, the proposed method is not so sensitive against the selection of the regularization parameters to some extent. However, those values are selected too big or too small, which would cause inappropriate regularized results.

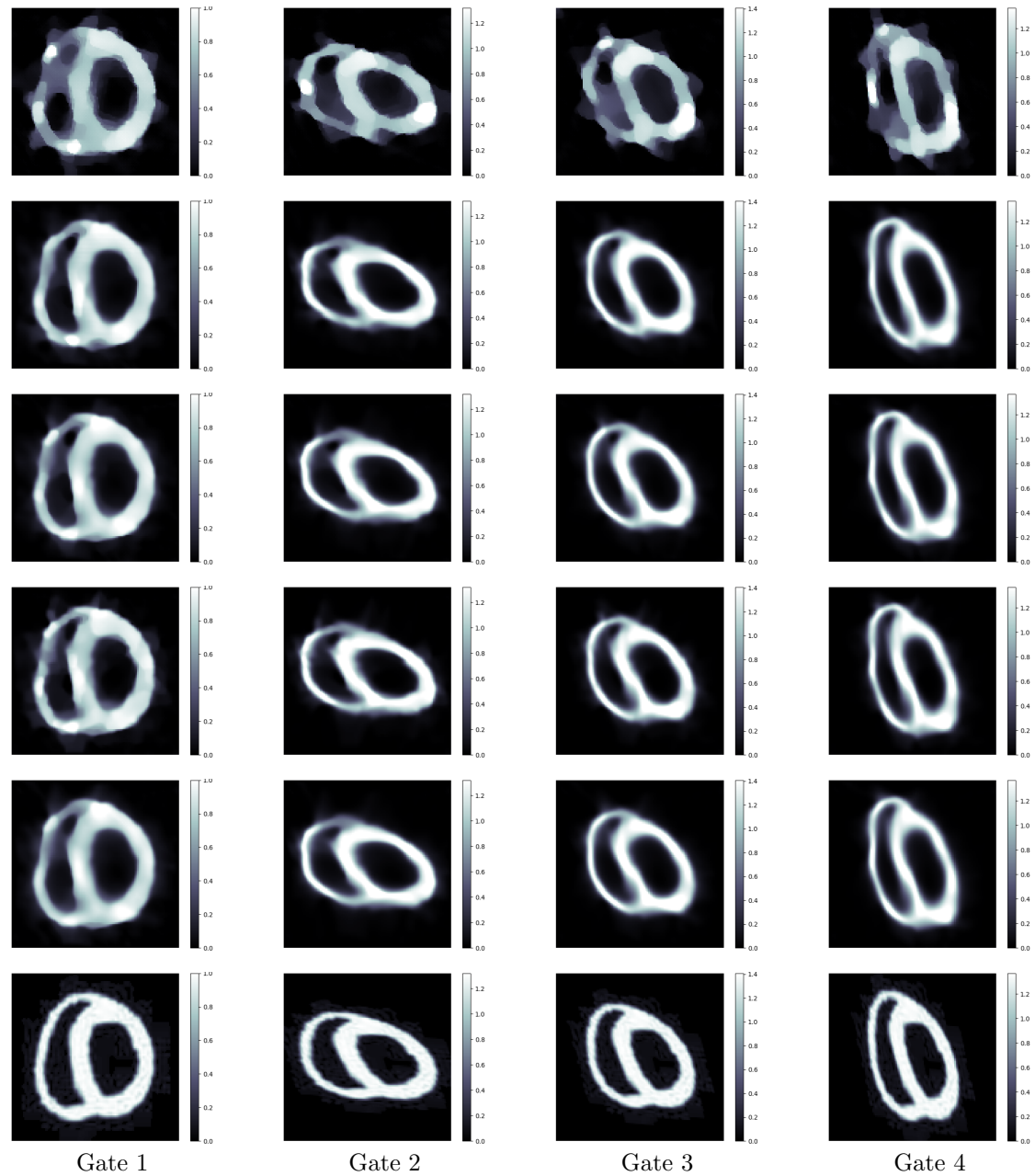


Fig. 7: Test suite 3. Reconstructed spatiotemporal images by selecting different regularization parameters. The columns represent the four gates. The first row shows the reconstructed images by TV-based method for each gate with  $\mu_1 = 0.02$ . The rows 2–5 respectively show the reconstructed spatiotemporal images by the proposed method with parameter pairs  $(\mu_1, \mu_2, \sigma)$  chosen as  $(0.02, 10^{-6}, 1.25)$ ,  $(0.02, 10^{-6}, 1.0)$ ,  $(0.01, 10^{-7}, 1.0)$ ,  $(0.03, 10^{-7}, 1.0)$ . The last row shows the ground truth of each gate.

	Gate 1	Gate 2	Gate 3	Gate 4
TV	0.6403	0.7054	0.6731	0.6671
	16.81	18.53	17.65	16.60
	0.3136	0.2964	0.3388	0.3773
Proposed	0.7603	0.7692	0.8102	0.8182
	20.18	21.95	23.15	23.01
	0.2127	0.2001	0.1798	0.1803
Proposed	0.7612	0.7525	0.7941	0.8083
	20.00	21.70	22.47	22.43
	0.2170	0.2058	0.1945	0.1927
Proposed	0.7485	0.7563	0.7998	0.8085
	19.83	21.89	22.45	22.20
	0.2215	0.2014	0.1949	0.1979
Proposed	0.7502	0.7560	0.7947	0.8021
	19.63	21.80	22.21	22.03
	0.2265	0.2034	0.2003	0.2019

Tab. 4: Test suite 3. The values of SSIM, PSNR and NRMSE of the reconstructed spatiotemporal images compared to the related ground truths for varying values of the regularization parameters  $\mu_1$ ,  $\mu_2$ , and the kernel width  $\sigma$ , see fig. 7 for the detailed images. Each entry has three values, where the upper is the value of SSIM, the middle is the value of PSNR, and the bottom is the value of NRMSE, which corresponds to the image on the counterpart position in fig. 7. Row 1: TV-based regularization method, and rows 2–5: The proposed method with different selecting parameters.

## 6 Discussion

Here we further discuss several important issues about the model and related algorithm.

### 6.1 An alternative model

As stated in the beginning of section 3, one method to ensure a Hilbert space being admissible is using the differential operator  $L$ . For instance, the presented model with ODE constraint in [16] can be written as

$$\begin{aligned} \min_{\substack{I \in \mathcal{X} \\ \nu \in \mathcal{L}_\gamma^2}} \int_0^1 \left[ \mathcal{D}_{\mathcal{T}_t, g_t}(\phi_{0,t}^\nu \cdot I) + \mu_2 \int_0^t \int_\Omega |L\nu(\tau, x)|^2 dx d\tau \right] dt + \mu_1 \mathcal{R}_1(I) \\ \text{s.t. } \phi_{0,t}^\nu \text{ solves ODE (13),} \end{aligned} \quad (59)$$

where (33) is the equivalent PDE-constrained optimal control formulation.

Inspired by the proposed model (22) and the model (59), an alternative model using the differential operator  $L$  is formulated as

$$\begin{aligned} \min_{\substack{I \in \mathcal{X} \\ \nu \in \mathcal{L}_\gamma^2}} \int_0^1 \left[ \mathcal{D}_{\mathcal{T}_t, g_t}(\phi_{0,t}^\nu \cdot I) + \mu_2 \int_0^t \int_\Omega \phi_{0,\tau}^\nu \cdot I(x) |L\nu(\tau, x)|^2 dx d\tau \right] dt + \mu_1 \mathcal{R}_1(I) \\ \text{s.t. } \phi_{0,t}^\nu \text{ solves ODE (13).} \end{aligned} \quad (60)$$

It is easy to obtain its equivalent PDE-constrained optimal control formulation. Furthermore, the time-discretized versions of (60) can be readily obtained following section 3.2.

Compared with (59), the unknown time-dependent image  $\phi_{0,\tau}^V \cdot I$  acting as the weight function is introduced into the shape regularization of (60). In contrast to (22), the differential operator  $L$  is explicitly used to construct that shape regularization. But these modifications would make the alternative model harder to solve. Through comparing with the models (22), (59) and (60), the relationship between LDDMM and optimal transportation becomes more clear.

## 6.2 Algorithmic initial values

Since the proposed model is nonlinear and nonconvex due to the composites of the template and diffeomorphic deformations (generated by the velocity field), the selection of algorithmic initial value has important influence on the final result.

During the implementation, it makes sense that the initial velocity field is always chosen as zero, and the resulting initial deformations are the identity deformation. That is because the optimal deformation is hopefully close to the identity deformation, which is characterized by the shape regularization in (22). Next we focus on the selection of the initial template. As we have tested by several examples in section 5, the selection of the initial template depends mainly on the degree of deformations of the ground truths at different gates. For instance in test suite 1, the deformation degree is relatively small, so we apply algorithm 1 to obtain an initial template after dozens of iterations by using all of the data with fixed zero velocity field. This means we treat the spatiotemporal reconstruction as a static one, and then use TV-regularization method to reconstruct. Even though the resulting initial template is blurring, it looks like the ground truth at the first gate and can be act as an appropriate initial value. On the other hand, if the deformation degree is relatively large as in test suite 3, the method above does not work because it would result in an initial template quite dissimilar as the ground truth at the first gate. Hence one alternative method is to employ algorithm 1 to gain an initial template by the projection data only at the first gate by sufficient iterations, then apply algorithm 2 to obtain an better initial velocity field by enough iterations based on the initial template above and initially zero velocity field. Finally, the applicable initial template and initial velocity field are obtained for the proposed algorithm.

## 6.3 The factor of discretized time degree

Another issue is the setting of the factor  $M$  of discretized time degree. As stated in section 4.4, this factor determines the discretized degree of each subinterval  $[t_i, t_{i+1}]$  for  $0 \leq i \leq N - 1$ . Setting  $M = 1$  means that the discretized time grid is coincident with the gating grid. For this case, the deformation of the images between adjacent gates is characterized by the linear displacement field from the view of numerical discretization. Besides that, the discretized time grid is finer than the gating grid by letting  $M > 1$ , which results in the deformation composited by multiple linear displacement fields (the number is  $M$ .) numerically.

As we have tested in section 5, the larger deformation or motion between the adjacent images, the lager  $M$  should be chosen. For example, we set  $M = 2$  in test suites 1 and 2, and let  $M = 8$  in test suite 3. That is because the deformation degree of the latter is larger than the former. However, we further found if the value of the factor has been set to be sufficiently large, using a larger one again would have no notable improvement for the ultimately results. In addition, the different subintervals of gating grid can be discretized adaptively according to the variability of motions.

## 6.4 Extended models

Inspired by the proposed model, we come up with several potential models also based on diffeomorphic optimal transportation.

**Image registration** Given the template image  $I_0: \Omega \rightarrow \mathbb{R}$  and the target image  $I_1: \Omega \rightarrow \mathbb{R}$ . Assume that they are both nonnegative and have the same mass. Using theorem 3, the variational model for image registration can be formulated as

$$\begin{aligned} \min_{\nu \in \mathcal{L}_\gamma^2} & \|\phi_{0,1}^\nu \cdot I_0 - I_1\|_2^2 + \mu \int_0^1 \int_\Omega \phi_{0,t}^\nu \cdot I_0(x) |\nu(t,x)|^2 dx dt \\ \text{s.t. } & \phi_{0,t}^\nu \text{ solves ODE (13),} \end{aligned} \quad (61)$$

where the  $\mu$  is the positive regularization parameter.

**Sequential image registration** Given the the time-series image  $I_{t_i}: \Omega \rightarrow \mathbb{R}$  for  $0 \leq t_i \leq 1$  and  $0 \leq i \leq N$ . Suppose that they are all nonnegative and have the same mass. The variational model for sequential image registration can be presented as

$$\begin{aligned} \min_{\nu \in \mathcal{L}_\gamma^2} & \frac{1}{N} \sum_{i=1}^N \left[ \|\phi_{0,t_i}^\nu \cdot I_{t_0} - I_{t_i}\|_2^2 + \mu \int_0^{t_i} \int_\Omega \phi_{0,\tau}^\nu \cdot I_{t_0}(x) |\nu(\tau,x)|^2 dx d\tau \right] \\ \text{s.t. } & \phi_{0,t}^\nu \text{ solves ODE (13).} \end{aligned} \quad (62)$$

The model (62) merely gives the time-discretized version for sequential image registration. The time-continuous version can be obtained naturally.

**Indirect image registration** Assume that the template image  $I_0: \Omega \rightarrow \mathbb{R}$  is given, and the indirect measurement  $g_1$  is obtained from the target image. Assume that both of the images are nonnegative and have the same mass. The variational model for indirect image registration can be formulated as

$$\begin{aligned} \min_{\nu \in \mathcal{L}_\gamma^2} & \|\mathcal{T}(\phi_{0,1}^\nu \cdot I_0) - g_1\|_2^2 + \mu \int_0^1 \int_\Omega \phi_{0,t}^\nu \cdot I_0(x) |\nu(t,x)|^2 dx dt \\ \text{s.t. } & \phi_{0,t}^\nu \text{ solves ODE (13).} \end{aligned} \quad (63)$$

Moreover, the case for sequentially indirect image registration has been already proposed in (38). Correspondingly, the time-continuous cases can be naturally achieved.

Note that the data fitting terms above can be modified according to the practical requirements. From the numerical point of view, the proposed algorithm in algorithm 2 can be simply adapted to solve the extended models (61)–(63). Therefore, if we consider the models with ODE-constrained formulation under appropriate conditions, the proposed algorithm provides a new scheme to solve the models based on  $\mathcal{L}^2$  Wasserstein distance in Benamou–Brenier formulation.

## 7 Conclusion

In this work, the  $\mathcal{L}^2$  Wasserstein distance in Benamou–Brenier formulation is used to characterize the optimal transport cost, and the unknown velocity field is restricted onto the admissible Hilbert space, which results in a diffeomorphic optimal transportation among the mass-preserving

image flows. Along the general framework for spatiotemporal imaging that presented in [16], a joint variational model has been investigated for the spatiotemporal image reconstruction with diffeomorphic and mass-preserving property. Therefore, the proposed model is a production of combining the Wasserstein distance of optimal transportation and the flow of diffeomorphisms involved in LDDMM, which is suitable for the scenario of spatiotemporal imaging with large diffeomorphic and mass-preserving deformations.

Additionally, the equivalent PDE-constrained optimal control formulation is obtained from the proposed model with ODE constraint. Using the PDE-constrained form, the proposed model has been theoretically compared against the existing joint variational model based on Wasserstein distance in [10], which demonstrates that the former can generate the sufficiently smooth velocity field, and further guarantee the flow of large non-rigid diffeomorphic deformations. And the optimal velocity field of the former is unnecessarily vanishing on the supports of the reconstructed images at the end time points, which implies the consistency between the time-continuous version and its associated time-discretized one. But those are not the cases for the model in [10] under appropriate conditions. Furthermore, the comparison is also performed for the proposed model in ODE-constrained form and the one based on the LDDMM consistent growth model proposed in our previous work [16], which makes clear the relationship between the optimal transportation and LDDMM.

The time-discretized versions with/without the ‘virtual’ template of the proposed model have also been presented, which are solved by the alternating minimization algorithm. Particularly, an alternating gradient descent algorithm was designed to solve the time-discretized proposed model with the ‘virtual’ template, where the most calculations only involve the easy-to-implement linearized deformations. Considering the gained ODE-constrained form under appropriate conditions, this algorithm provides a new idea to solve the other models based on  $\mathcal{L}^2$  Wasserstein distance in Benamou–Brenier formulation.

The performance of the proposed model and associated algorithm is finally validated by several numerical experiments in 2D space and time tomography with sparse-view and/or different noise level data measured from topology-preserving and mass-preserving sequential images. Using the noise-free and sparse-view projection data, we evaluated the overview performance of the proposed method, including numerical convergence, reconstructed image quality, and mass-preserving property. The numerical results have showed the desirable performance with respect to those aspects. In particular, the proposed method has much better reconstruction accuracy than the  $\mathcal{L}^2$ -gradient descent scheme and the TV-regularization method from both the visual and quantitative perspectives. And the proposed method generated smooth optimal velocity field, but that is not the case of the  $\mathcal{L}^2$ -gradient descent scheme.

Moreover, we have tested the robustness against the different noise levels for the proposed method. Even if the projection data is disturbed by different noise levels, the proposed method can always track the motions of the objects and reconstruct more accurate sequential images. Through the numerical validation, we also found that the proposed method is not so sensitive against the selection of the related regularization parameters. Conclusively, the proposed method can stably improve the quality of the reconstructed images in spatiotemporal imaging with large diffeomorphic and mass-preserving deformations.

We further made a lot of important discussions about the proposed model and algorithms. Particularly, an alternative model was proposed for spatiotemporal imaging, which is also coupled the thoughts of LDDMM and optimal transportation. Although this alternative is more complicated than the proposed one, it might have some potential application. Illustrating with the different numerical tests, we also analyzed the selections of algorithmic initial value and the factor of discretized time degree, which provides the guidelines for the numerical implementation of the proposed model. Inspired by the proposed model, we came up with several extended

models with applications to more image processing and biomedical imaging. Importantly, the proposed algorithm provides a new scheme to solve the models based on  $\mathcal{L}^2$  Wasserstein distance in Benamou–Brenier formulation.

We are going to concern the more theoretical aspects of the proposed model and algorithms, the further extensions following the studied framework, and the applications and related theory to more spatiotemporal biomedical imaging and image processing.

## A Optimality conditions

The optimality conditions for (22) and (25). Let us begin with the following lemma.

**Lemma 1.** *Let  $\nu, \eta \in \mathcal{L}_{\mathcal{V}}^2$ , and  $\phi_{0,t}^{\nu}$  denote the solution to the ODE in (13) with given  $\nu$ , and  $I \in \mathcal{L}^2(\Omega, \mathbb{R})$  be differentiable. Using the mass-preserving deformation in (4), then*

$$\frac{d}{d\epsilon} (\phi_{0,t}^{\nu+\epsilon\eta} \cdot I)(x) \Big|_{\epsilon=0} = |D(\phi_{t,0}^{\nu})(x)| \operatorname{div}(I h_{t,0}^{\nu}) \circ \phi_{t,0}^{\nu}(x) \quad (64)$$

for  $x \in \Omega$  and  $0 \leq t \leq 1$ , where

$$h_{t,0}^{\nu} = - \int_0^t D(\phi_{\tau,0}^{\nu})(\phi_{0,\tau}^{\nu}) \left( \eta(\tau, \phi_{0,\tau}^{\nu}) \right) d\tau. \quad (65)$$

*Proof.* By the mass-preserving deformation in (4), and using (18), we have

$$\frac{d}{d\epsilon} (\phi_{0,t}^{\nu+\epsilon\eta} \cdot I)(x) \Big|_{\epsilon=0} = \frac{d}{d\epsilon} |D(\phi_{t,0}^{\nu+\epsilon\eta})(x)| I \circ \phi_{t,0}^{\nu+\epsilon\eta}(x) \Big|_{\epsilon=0}.$$

Using the result from [16, Lemma A.1], then

$$\frac{d}{d\epsilon} \phi_{t,0}^{\nu+\epsilon\eta}(x) \Big|_{\epsilon=0} = h_{t,0}^{\nu} \circ \phi_{t,0}^{\nu}(x).$$

Following the proof of [17, Theorem 8.3], we have

$$\frac{d}{d\epsilon} |D(\phi_{t,0}^{\nu+\epsilon\eta})(x)| \Big|_{\epsilon=0} = |D(\phi_{t,0}^{\nu})(x)| \operatorname{div}(h_{t,0}^{\nu}) \circ \phi_{t,0}^{\nu}(x).$$

By the chain rule we obtain the result of (64).  $\square$

Then the following result is obtained immediately.

**Lemma 2.** *Let the assumptions in lemma 1 hold and  $\mathcal{D}_{\mathcal{T}_t, g_t}: \mathcal{X} \rightarrow \mathbb{R}$  be defined as (6). Assuming that  $\mathcal{D}_{\mathcal{T}_t, g_t}$  is differentiable. Then*

$$\frac{d}{d\epsilon} \mathcal{D}_{\mathcal{T}_t, g_t}(\phi_{0,t}^{\nu+\epsilon\eta} \cdot I) \Big|_{\epsilon=0} = \int_0^t \left\langle \phi_{0,\tau}^{\nu} \cdot I \nabla \left( \partial \mathcal{D}_{\mathcal{T}_t, g_t}(\phi_{0,t}^{\nu} \cdot I)(\phi_{\tau,t}^{\nu}) \right), \eta(\tau, \cdot) \right\rangle_{\mathcal{L}^2(\Omega, \mathbb{R}^n)} d\tau, \quad (66)$$

where  $\partial \mathcal{D}_{\mathcal{T}_t, g_t}$  represents the gradient of  $\mathcal{D}_{\mathcal{T}_t, g_t}$ .

In what follows we derive the optimality conditions for (22).

**Theorem 6.** *Let the assumptions in lemma 2 hold and  $\mathcal{E}_C: \mathcal{X} \times \mathcal{L}_{\mathcal{V}}^2 \rightarrow \mathbb{R}$  denote the objective functional in (22) of time-continuous version, i.e.,*

$$\mathcal{E}_C(I, \nu) := \int_0^1 \left[ \mathcal{D}_{\mathcal{T}_t, g_t}(\phi_{0,t}^{\nu} \cdot I) + \mu_2 \int_0^t \int_{\Omega} \phi_{0,\tau}^{\nu} \cdot I(x) |\nu(\tau, x)|^2 dx d\tau \right] dt + \mu_1 \mathcal{R}_1(I). \quad (67)$$

Assume that the regularization term  $\mathcal{R}_1$  is differentiable, and  $\mathcal{V}$  is an RKHS with a reproducing kernel  $\mathbf{K}: \Omega \times \Omega \rightarrow \mathbb{M}_+^{d \times d}$ . Then the gradient (i.e.,  $\mathcal{L}^2$ -gradient) with regard to the velocity field  $\boldsymbol{\nu}$  of  $\mathcal{E}_C(I, \cdot)$  is

$$\begin{aligned} \nabla_{\boldsymbol{\nu}} \mathcal{E}_C(I, \boldsymbol{\nu})(t, \cdot) &= \phi_{0,t}^{\boldsymbol{\nu}} \cdot I \int_t^1 \nabla \left( \left[ \partial \mathcal{D}_{\mathcal{T}_\tau, g_\tau}(\phi_{0,\tau}^{\boldsymbol{\nu}} \cdot I) + \mu_2(1-\tau) |\boldsymbol{\nu}(\tau, \cdot)|^2 \right] (\phi_{t,\tau}^{\boldsymbol{\nu}}) \right) d\tau \\ &\quad + 2\mu_2(1-t) \phi_{0,t}^{\boldsymbol{\nu}} \cdot I \boldsymbol{\nu}(t, \cdot) \end{aligned} \quad (68)$$

and the  $\mathcal{L}_{\mathcal{V}}^2$ -gradient with regard to the velocity field  $\boldsymbol{\nu}$  of  $\mathcal{E}_C(I, \cdot)$  is

$$\begin{aligned} \nabla_{\boldsymbol{\nu}}^{\mathcal{V}} \mathcal{E}_C(I, \boldsymbol{\nu})(t, \cdot) &= \mathcal{K} \left( \phi_{0,t}^{\boldsymbol{\nu}} \cdot I \int_t^1 \nabla \left( \left[ \partial \mathcal{D}_{\mathcal{T}_\tau, g_\tau}(\phi_{0,\tau}^{\boldsymbol{\nu}} \cdot I) + \mu_2(1-\tau) |\boldsymbol{\nu}(\tau, \cdot)|^2 \right] (\phi_{t,\tau}^{\boldsymbol{\nu}}) \right) d\tau \right. \\ &\quad \left. + 2\mu_2(1-t) \phi_{0,t}^{\boldsymbol{\nu}} \cdot I \boldsymbol{\nu}(t, \cdot) \right) \end{aligned} \quad (69)$$

for  $0 \leq t \leq 1$  and where  $\mathcal{K}(\varphi) = \int_{\Omega} \mathbf{K}(\cdot, y) \varphi(y) dy$ . Moreover, the gradient with regard to the template  $I$  of  $\mathcal{E}_C(\cdot, \boldsymbol{\nu})$  is

$$\nabla_I \mathcal{E}_C(I, \boldsymbol{\nu}) = \int_0^1 \left[ \partial \mathcal{D}_{\mathcal{T}_t, g_t}(\phi_{0,t}^{\boldsymbol{\nu}} \cdot I) + \mu_2(1-t) |L\boldsymbol{\nu}(t, \cdot)|^2 \right] (\phi_{0,t}^{\boldsymbol{\nu}}) dt + \mu_1 \partial \mathcal{R}_1(I), \quad (70)$$

where  $\partial \mathcal{R}_1$  denotes the gradient of  $\mathcal{R}_1: \mathcal{X} \rightarrow \mathbb{R}$ . The optimality conditions for (22) are formulated as

$$\begin{cases} \nabla_{\boldsymbol{\nu}}^{\mathcal{V}} \mathcal{E}_C(I, \boldsymbol{\nu}) = 0, \\ \nabla_I \mathcal{E}_C(I, \boldsymbol{\nu}) - \lambda = 0, \\ \lambda \geq 0, \quad I \geq 0, \quad \lambda I = 0, \end{cases} \quad (71)$$

where  $\lambda$  denotes the Lagrange multiplier.

*Proof.* Applying the results in lemma 1 and lemma 2, we immediately have

$$\begin{aligned} \frac{d}{d\epsilon} \mathcal{E}_C(I, \boldsymbol{\nu} + \epsilon \boldsymbol{\eta}) \Big|_{\epsilon=0} &= \int_0^1 \int_0^t \left\langle \phi_{0,\tau}^{\boldsymbol{\nu}} \cdot I \nabla \left( \partial \mathcal{D}_{\mathcal{T}_t, g_t}(\phi_{0,t}^{\boldsymbol{\nu}} \cdot I) (\phi_{\tau,t}^{\boldsymbol{\nu}}) \right), \boldsymbol{\eta}(\tau, \cdot) \right\rangle_{\mathcal{L}^2(\Omega, \mathbb{R}^n)} d\tau dt \\ &\quad + \mu_2 \int_0^1 \int_0^t \int_0^\tau \left\langle \phi_{0,t}^{\boldsymbol{\nu}} \cdot I \nabla \left( |L\boldsymbol{\nu}(\tau, \cdot)|^2 (\phi_{t,\tau}^{\boldsymbol{\nu}}) \right), \boldsymbol{\eta}(t, \cdot) \right\rangle_{\mathcal{L}^2(\Omega, \mathbb{R}^n)} dt d\tau dt \\ &\quad + 2\mu_2 \int_0^1 \int_0^t \left\langle \phi_{0,\tau}^{\boldsymbol{\nu}} \cdot I \boldsymbol{\nu}(\tau, \cdot), \boldsymbol{\eta}(\tau, \cdot) \right\rangle_{\mathcal{L}^2(\Omega, \mathbb{R}^n)} d\tau dt. \end{aligned}$$

Changing the order of integration in the above equation gives

$$\begin{aligned} \frac{d}{d\epsilon} \mathcal{E}_C(I, \boldsymbol{\nu} + \epsilon \boldsymbol{\eta}) \Big|_{\epsilon=0} &= \int_0^1 \left\langle \phi_{0,\tau}^{\boldsymbol{\nu}} \cdot I \int_\tau^1 \nabla \left( \partial \mathcal{D}_{\mathcal{T}_t, g_t}(\phi_{0,t}^{\boldsymbol{\nu}} \cdot I) (\phi_{\tau,t}^{\boldsymbol{\nu}}) \right) dt, \boldsymbol{\eta}(\tau, \cdot) \right\rangle_{\mathcal{L}^2(\Omega, \mathbb{R}^n)} d\tau \\ &\quad + \mu_2 \int_0^1 \left\langle \phi_{0,\tau}^{\boldsymbol{\nu}} \cdot I \int_\tau^1 (1-t) \nabla \left( |L\boldsymbol{\nu}(t, \cdot)|^2 (\phi_{t,\tau}^{\boldsymbol{\nu}}) \right) dt, \boldsymbol{\eta}(\tau, \cdot) \right\rangle_{\mathcal{L}^2(\Omega, \mathbb{R}^n)} d\tau \\ &\quad + 2\mu_2 \int_0^1 \left\langle (1-\tau) \phi_{0,\tau}^{\boldsymbol{\nu}} \cdot I \boldsymbol{\nu}(\tau, \cdot), \boldsymbol{\eta}(\tau, \cdot) \right\rangle_{\mathcal{L}^2(\Omega, \mathbb{R}^n)} d\tau. \end{aligned} \quad (72)$$

As  $\mathcal{V}$  is an RKHS with a reproducing kernel represented by  $\mathbb{K}: \Omega \times \Omega \rightarrow \mathbb{M}_+^{n \times n}$ , then

$$\langle \nu, \eta \rangle_{\mathcal{L}^2(\Omega, \mathbb{R}^n)} = \left\langle \int_{\Omega} \mathbb{K}(\cdot, y) \nu(y) dy, \eta \right\rangle_{\mathcal{V}} \quad \text{for } \nu, \eta \in \mathcal{V}. \quad (73)$$

Using (72) and (73), we prove (69). Moreover, it is simple to obtain the results of (70) and (71). Therefore their proofs are omitted.  $\square$

For simplicity, let us introduce the following notation

$$h_{\tau, t}^{I, \nu} := \begin{cases} \partial \mathcal{D}_{\mathcal{T}_\tau, g_t}(\phi_{0, t}^\nu \cdot I)(\phi_{\tau, t}^\nu), & 0 \leq \tau \leq t \leq 1, \\ 0, & t < \tau, \end{cases} \quad (74)$$

$$\eta_{\tau, t}^\nu := \begin{cases} \int_{\tau}^t |\nu(t, \cdot)|^2(\phi_{\tau, t}^\nu) dt, & 0 \leq \tau \leq t \leq 1, \\ 0, & t < \tau, \end{cases} \quad (75)$$

$$\nu_{\tau, t} := \begin{cases} \nu(\tau, \cdot), & 0 \leq \tau \leq t \leq 1, \\ 0, & t < \tau. \end{cases} \quad (76)$$

**Theorem 7.** *Let the assumptions in theorem 6 hold and  $\mathcal{E}_D: \mathcal{X} \times \mathcal{L}_{\mathcal{V}}^2 \rightarrow \mathbb{R}$  denote the objective functional in (25) of time-discretized version, i.e.,*

$$\mathcal{E}_D(I, \nu) := \frac{1}{N} \sum_{i=1}^N \left[ \mathcal{D}_{\mathcal{T}_{t_i}, g_{t_i}}(\phi_{0, t_i}^\nu \cdot I) + \mu_2 \int_0^{t_i} \int_{\Omega} \phi_{0, \tau}^\nu \cdot I(x) |\nu(\tau, x)|^2 dx d\tau \right] + \mu_1 \mathcal{R}_1(I). \quad (77)$$

The gradient of  $\mathcal{E}_D$  with regard to the velocity field  $\nu$  is

$$\nabla_{\nu} \mathcal{E}_D(I, \nu) = \frac{1}{N} \sum_{\{i \geq 1: t_i \geq t\}} \left( \phi_{0, t}^\nu \cdot I \left[ \nabla(h_{t, t_i}^{I, \nu} + \mu_2 \eta_{t, t_i}^\nu) + 2\mu_2 \nu_{t, t_i} \right] \right) \quad (78)$$

and the  $\mathcal{L}_{\mathcal{V}}^2$ -gradient of  $\mathcal{E}_D$  with regard to the velocity field  $\nu$  is

$$\nabla_{\nu}^{\mathcal{L}_{\mathcal{V}}^2} \mathcal{E}_D(I, \nu) = \frac{1}{N} \sum_{\{i \geq 1: t_i \geq t\}} \mathcal{K} \left( \phi_{0, t}^\nu \cdot I \left[ \nabla(h_{t, t_i}^{I, \nu} + \mu_2 \eta_{t, t_i}^\nu) + 2\mu_2 \nu_{t, t_i} \right] \right). \quad (79)$$

Moreover, the gradient of  $\mathcal{E}_D$  with regard to the template  $I$  is

$$\nabla_I \mathcal{E}_D(I, \nu) = \frac{1}{N} \sum_{i=1}^N (h_{0, t_i}^{I, \nu} + \mu_2 \eta_{0, t_i}^\nu) + \mu_1 \partial \mathcal{R}_1(I). \quad (80)$$

Consequently, the optimality conditions for (77) are formulated as

$$\begin{cases} \nabla_{\nu}^{\mathcal{L}_{\mathcal{V}}^2} \mathcal{E}_D(I, \nu) = 0, \\ \nabla_I \mathcal{E}_D(I, \nu) - \lambda = 0, \\ \lambda \geq 0, \quad I \geq 0, \quad \lambda I = 0, \end{cases} \quad (81)$$

where  $\lambda$  denotes the Lagrange multiplier.

*Proof.* By lemma 1, we derive

$$\begin{aligned}
\frac{d}{d\epsilon} \mathcal{E}_D(I, \nu + \epsilon \eta) \Big|_{\epsilon=0} &= \frac{1}{N} \sum_{i=1}^N \int_0^{t_i} \left\langle \phi_{0,\tau}^\nu \cdot I \nabla \left( \partial \mathcal{D}_{\tau_i, g_{t_i}}(\phi_{0,t_i}^\nu \cdot I)(\phi_{\tau,t_i}^\nu) \right), \eta(\tau, \cdot) \right\rangle_{\mathcal{L}^2(\Omega, \mathbb{R}^n)} d\tau \\
&+ \frac{\mu_2}{N} \sum_{i=1}^N \int_0^{t_i} \int_0^\tau \left\langle \phi_{0,t}^\nu \cdot I \nabla \left( |L\nu(\tau, \cdot)|^2(\phi_{t,\tau}^\nu) \right), \eta(t, \cdot) \right\rangle_{\mathcal{L}^2(\Omega, \mathbb{R}^n)} dt d\tau \\
&+ \frac{2\mu_2}{N} \sum_{i=1}^N \int_0^{t_i} \left\langle \phi_{0,\tau}^\nu \cdot I \nu(\tau, \cdot), \eta(\tau, \cdot) \right\rangle_{\mathcal{L}^2(\Omega, \mathbb{R}^n)} d\tau \\
&= \int_0^1 \left\langle \frac{1}{N} \sum_{\{i \geq 1: t_i \geq t\}} \phi_{0,t}^\nu \cdot I \nabla h_{t,t_i}^{I,\nu}, \eta(t, \cdot) \right\rangle_{\mathcal{L}^2(\Omega, \mathbb{R}^n)} dt \\
&+ \int_0^1 \left\langle \frac{\mu_2}{N} \sum_{\{i \geq 1: t_i \geq t\}} \phi_{0,t}^\nu \cdot I \nabla \eta_{t,t_i}^\nu, \eta(t, \cdot) \right\rangle_{\mathcal{L}^2(\Omega, \mathbb{R}^n)} dt \\
&\quad + \int_0^1 \left\langle \frac{2\mu_2}{N} \sum_{\{i \geq 1: t_i \geq t\}} \nu_{t,t_i} \phi_{0,t}^\nu \cdot I, \eta(t, \cdot) \right\rangle_{\mathcal{L}^2(\Omega, \mathbb{R}^n)} dt.
\end{aligned}$$

Using (74)–(76), the last equation is achieved. Using (73) and the obtained result above, we prove (79). Moreover, the result of (80) is straightforward.  $\square$

## References

- [1] L. Ambrosio. Lecture notes on optimal transport problems. In *Mathematical Aspects of Evolving Interfaces*, volume 1812 of *Lecture Notes in Mathematics*, pages 1–52. Springer-Verlag, Berlin, 2003.
- [2] M. Arjovsky, S. Chintala, and L. Bottou. Wasserstein GAN. arXiv:1701.07875, 2017.
- [3] N. Aronszajn. Theory of reproducing kernels. *Transactions of the American Mathematical Society*, 68(3):337–404, 1950.
- [4] W. Bai and M. Brady. Motion correction and attenuation correction for respiratory gated PET images. *IEEE Trans. Med. Imaging*, 30(2):351–365, 2011.
- [5] F. M. Beg, M. I. Miller, A. Trounev, and L. Younes. Computing large deformation metric mappings via geodesic flow of diffeomorphisms. *International Journal of Computer Vision*, 61(2):139–157, 2005.
- [6] J.-D. Benamou and Y. Brenier. A computational fluid mechanics solution to the Monge-Kantorovich mass transfer problem. *Numerische Mathematik*, 84(3):375–393, 2000.
- [7] M. Blume, N. Navab, and M. Rafecas. Joint image and motion reconstruction for PET using a B-spline motion model. *Phys. Med. Biol.*, 57(24):8249–8270, 2012.
- [8] A. Bousse, O. Bertolli, D. Atkinson, S. Arridge, S. Ourselin, B. F. Hutton, and S. Thielemans. Maximum-Likelihood Joint Image Reconstruction/Motion Estimation in Attenuation-Corrected Respiratory Gated PET/CT Using a Single Attenuation Map. *IEEE Transactions on Medical Imaging*, 35(1):217–228, 2016.

- [9] M. Brehm, S. Sawall, J. Maier, S. Sauppe, and M. Kachelriess. Cardiorespiratory motion-compensated micro-CT image reconstruction using an artifact model-based motion estimation. *Med. Phys.*, 42(4):1948–1958, 2015.
- [10] C. Brune. *4D Imaging in Tomography and Optical Nanoscopy*. PhD thesis, University of Münster, Münster, Germany, 2010.
- [11] M. Bruveris and D. D. Holm. Geometry of image registration: The diffeomorphism group and momentum maps. In Chang D. E., D. D. Holm, G. Patrick, and T. Ratiu, editors, *Geometry, Mechanics, and Dynamics: The Legacy of Jerry Marsden*, volume 73 of *Fields Institute Communications*, pages 19–56. Springer-Verlag, 2015.
- [12] M. Burger, H. Dirks, L. Frerking, A. Hauptmann, T. Helin, and S. Siltanen. A variational reconstruction method for undersampled dynamic x-ray tomography based on physical motion models. *Inverse Problems*, 33(12):124008 (24pp), 2017.
- [13] M. Burger, H. Dirks, and C. Schönlieb. A Variational Model for Joint Motion Estimation and Image Reconstruction. *SIAM Journal on Imaging Sciences*, 11(1):94–128, 2018.
- [14] M. Burger, J. Modersitzki, and L. Ruthotto. A Hyperelastic Regularization Energy for Image Registration. *SIAM J. Sci. Comput.*, 35(1):B132–B148, 2013.
- [15] F. Büther, M. Dawood, L. Stegger, F. Wübbeling, M. Schäfers, O. Schober, and K. P. Schäfers. List mode-driven cardiac and respiratory gating in PET. *J. Nucl. Med.*, 50(5):674–681, 2009.
- [16] C. Chen, B. Gris, and O. Öktem. A New Variational Model for Joint Image Reconstruction and Motion Estimation in Spatiotemporal Imaging. *SIAM Journal on Imaging Sciences*, 12(4):1686–1719, 2019.
- [17] C. Chen and O. Öktem. Indirect Image Registration with Large Diffeomorphic Deformations. *SIAM Journal on Imaging Sciences*, 11(1):575–617, 2018.
- [18] M. Dawood, F. Büther, X. Jiang, and K. P. Schäfers. Respiratory motion correction in 3-D PET data with advanced optical flow algorithms. *IEEE Trans. Med. Imaging*, 27(8):1164–1175, 2008.
- [19] M. Dawood, F. Büther, N. Lang, O. Schober, and K. P. Schäfers. Respiratory gating in positron emission tomography: a quantitative comparison of different gating schemes. *Med. Phys.*, 34(7):3067–3076, 2007.
- [20] M. Dawood, N. Lang, X. Jiang, and K. P. Schäfers. Lung motion correction on respiratory gated 3-D PET/CT images. *IEEE Trans. Med. Imaging*, 25:1164–1175, 2006.
- [21] M. Dawood, L. Stegger, X. Jiang, O. Schober, M. Schäfers, and K. P. Schäfers. Optimal number of respiratory gates in positron emission tomography: a cardiac patient study. *Med. Phys.*, 36(5):1775–1784, 2009.
- [22] P. Dupuis, U. Grenander, and M. Miller. Variational Problems on Flows of Diffeomorphisms for Imaging Matching. *Quarterly of Applied Mathematics*, 56(3):587–600, 1998.
- [23] B. Engquist and B. Froese. Application of the Wasserstein metric to seismic signals. *Commun. Math. Sci.*, 12:979–988, 2014.

- [24] H. Gao, J. Cai, Z. Shen, and H. Zhao. Robust principal component analysis-based four-dimensional computed tomography. *Phys. Med. Biol.*, 56:3181–3198, 2011.
- [25] F. Gigengack, X. Jiang, M. Dawood, and K. Schäfers. *Motion Correction in Thoracic Position Emission Tomography*. Springer Briefs in Electrical and Computer Engineering. Springer, 2015.
- [26] F. Gigengack, L. Ruthotto, M. Burger, C. H. Wolters, X. Jiang, and K. P. Schäfers. Motion correction in dual gated cardiac PET using mass-preserving image registration. *IEEE Trans. Med. Imaging*, 31(3):698–712, 2012.
- [27] U. Grenander and M. Miller. *Pattern Theory. From Representation to Inference*. Oxford University Press, 2007.
- [28] B. Gris, C. Chen, and O. Öktem. Image reconstruction through metamorphosis. *Inverse Problems*, 36(2):025001 (27pp), 2020.
- [29] W. Grootjans, L.-F. de Geus-Oei, A. P. W. Meeuwis, S. Charlotte, M. Gotthardt, W. Oyen, and E. Visser. Amplitude-based optimal respiratory gating in positron emission tomography in patients with primary lung cancer. *Eur. Radio.*, 24(12):3242–3250, 2014.
- [30] S. Haker, L. Zhu, A. Tannenbaum, and S. Angenent. Optimal mass transport for registration and warping. *Int. J. Comput. Vis.*, 60:225–240, 2004.
- [31] J. P. Haldar and Z.-P. Liang. Spatiotemporal Imaging with Partially Separable Functions: A Matrix Recovery Approach. In *Proc. IEEE Int'l Symposium Biomedical Imaging*, pages 716–719, 2010.
- [32] J. Hinkle, M. Szegedi, B. Wang, B. Salter, and S. Joshi. 4D CT image reconstruction with diffeomorphic motion model. *Medical Image Analysis*, 16(6):1307–1316, 2012.
- [33] X. Jia, Y. Lou, B. Dong, Z. Tian, and S. Jiang. 4D computed tomography reconstruction from few-projection data via temporal non-local regularization. In T. Jiang, N. Navab, J. Pluim, and M. Viergever, editors, *Medical Image Computing and Computer-Assisted Intervention – MICCAI 2010*, volume 6361 of *Lecture Notes in Computer Science*, pages 143–150. Springer-Verlag, 2010.
- [34] L. V. Kantorovich. On the problem of Monge. *Uspekhi Mat. Nauk.*, 3:225–226, 1948.
- [35] J. Karlsson and A. Ringh. Generalized Sinkhorn iterations for regularizing inverse problems using optimal mass transport. *SIAM J. Imaging Sciences*, 10(4):1935–1962, 2017.
- [36] N. Lang, M. Dawood, F. Büther, O. Schober, M. Schäfers, and K. P. Schäfers. Organ movement reduction in PET/CT using dual-gated list-mode acquisition. *Med. Phys.*, 16(1):93–100, 2006.
- [37] Z.-P. Liang and P. C. Lauterbur. *Principles of Magnetic Resonance Imaging: A Signal Processing Perspective*. IEEE Press/John Wiley, 1999.
- [38] J. Liu, X. Zhang, H. Zhao, Y. Gao, D. Thomas, D. Low, and H. Gao. 5D respiratory motion model based image reconstruction algorithm for 4D cone-beam computed tomography. *Inverse Problems*, 31:115007, 2015.
- [39] G. Lucignani. Respiratory and cardiac motion correction with 4D PET imaging: shooting at moving targets. *Eur. J. Nucl. Med. Mol. Imaging*, 36(2):315–319, 2009.

- [40] F. Lucka, N. Huynh, M. Betcke, E. Zhang, P. Beard, B. Cox, and S. Arridge. Enhancing Compressed Sensing 4D Photoacoustic Tomography by Simultaneous Motion Estimation. *SIAM J. Imaging Sciences*, 11(4):2224–2253, 2018.
- [41] J. Maas, M. Rumpf, C. Schönlieb, and S. Simon. A generalized model for optimal transport of images including dissipation and density modulation. *ESAIM: Mathematical Modelling and Numerical Analysis*, 49(6):1745–1769, 2015.
- [42] M. I. Miller, A. Trouvé, and L. Younes. On the metrics and Euler-Lagrange equations of computational anatomy. *Annual Reviews of Biomedical Engineering*, 4:375–405, 2002.
- [43] G. Monge. Mémoire sur la théorie des déblais et des remblais. *Histoire de l’Académie Royale des Science, Année 1781, avec les Mémoires de Mathématique et de Physique*, 1781.
- [44] F. Natterer. *The Mathematics of Computerized Tomography*, volume 32 of *Classics in Applied Mathematics*. SIAM, 2001.
- [45] O. Öktem, C. Chen, N. O. Domaniç, P. Ravikumar, and C. Bajaj. Shape based image reconstruction using linearised deformations. *Inverse Problems*, 33(3):035004, 2017.
- [46] G. Peyré and M. Cuturi. Computational Optimal Transport. arXiv:1803.00567, 2018.
- [47] A. Rahmim, J. Tang, and H. Zaidi. Four-Dimensional Image Reconstruction Strategies in Cardiac-Gated and Respiratory-Gated PET Imaging. *PET Clin.*, 8(1):51–67, 2013.
- [48] L. Ritschl, S. Sawall, M. Knaup, A. Hess, and M. Kachelriess. Iterative 4D cardiac micro-CT image reconstruction using an adaptive spatio-temporal sparsity prior. *Phys. Med. Biol.*, 57:1517–1525, 2012.
- [49] H. Schumacher, J. Modersitzki, and B. Fischer. Combined reconstruction and motion correction in SPECT imaging. *IEEE Trans. Nucl. Sci.*, 56:73–80, 2009.
- [50] T. Schuster, B. Hahn, and M. Burger. Dynamic inverse problems: modelling—regularization—numerics. *Inverse Problems*, 34(4):040301 (4pp), 2018.
- [51] A. J. Schwarz and M. O. Leach. Implications of respiratory motion for the quantification of 2D MR spectroscopic imaging data in the abdomen. *Phys. Med. Biol.*, 45(8):2105–2116, 2000.
- [52] Q. Tang, J. Cammin, S. Srivastava, and K. Taguchi. A fully four-dimensional, iterative motion estimation and compensation method for cardiac CT. *Med. Phys.*, 39(7):4291–4305, 2012.
- [53] D’Arcy Thompson. *On Growth and Form*. Cambridge University Press, New York, 1945.
- [54] A. Trouvé. Diffeomorphisms Groups and Pattern Matching in Imaging Analysis. *International Journal of Computer Vision*, 28(3):213–221, 1998.
- [55] C. Villani. *Topics in Optimal Transportation*, volume 58 of *Graduate Studies in Mathematics*. American Mathematics Society, 2003.
- [56] Y. Wang, E. Vidan, and G. W. Bergman. Cardiac motion of coronary arteries: variability in the rest period and implications for coronary MR angiography. *Radiology*, 213(3):751–758, 1999.

- 
- [57] Z. Wang, A. C. Bovik, H. R. Sheikh, and E. P. Simoncelli. Image quality assessment: From error visibility to structural similarity. *IEEE Trans. Image Process.*, 13:600–612, 2004.
- [58] L. Younes. *Shapes and Diffeomorphisms*, volume 171 of *Applied Mathematical Sciences*. Springer-Verlag, 2010.